

Repeating flares, X-ray outbursts and delayed infrared emission: A comprehensive compilation of optical tidal disruption events

TDECat

D. A. Langis^{1,2,*}, I. Liodakis^{1,3}, K. I. I. Koljonen⁴, A. Paggi¹, N. Globus^{5,6}, L. Wyrzykowski^{7,8},
P. J. Mikołajczyk^{7,8,9}, K. Kotysz^{7,9}, P. Zieliński¹⁰, N. Ihanec^{11,7}, J. Ding^{12,13}, D. Morshed¹⁴, and Z. Torres¹⁵

¹ Institute of Astrophysics, FORTH, N.Plastira 100, Vassilika Vouton, 70013 Heraklion, Greece

² Department of Physics, University of Crete, 71003 Heraklion, Greece

³ NASA Marshall Space Flight Center, Huntsville, AL 35812, USA

⁴ Institutt for Fysikk, Norwegian University of Science and Technology, Høgskoleringen 5, Trondheim 7491, Norway

⁵ Instituto de Astronomía, Universidad Nacional Autónoma de México Campus Ensenada, Carr. Tijuana-Ensenada km107, Ensenada, BC 22800, Mexico

⁶ Kavli Institute for Particle Astrophysics and Cosmology, Stanford University, Stanford, CA 94305, USA

⁷ Astronomical Observatory, University of Warsaw, Al. Ujazdowskie 4, 00-478 Warszawa, Poland

⁸ Astrophysics Division, National Centre for Nuclear Research, Pasteura 7, 02-093 Warsaw, Poland

⁹ Astronomical Institute, University of Wrocław, Kopernika 11, 51-622 Wrocław, Poland

¹⁰ Institute of Astronomy, Faculty of Physics, Astronomy and Informatics, Nicolaus Copernicus University, Grudziądzka 5, 87-100 Toruń, Poland

¹¹ Isaac Newton Group of Telescopes, Apartado 321, E-38700 Santa Cruz de la Palma, Spain

¹² Princeton University, Princeton, NJ 08544, USA

¹³ Rye Country Day School, NY 10580, USA

¹⁴ Head-Royce School, CA 94602, USA

¹⁵ Harbor High School, CA 95062, USA

Received 31 March 2025 / Accepted 14 December 2025

ABSTRACT

Tidal disruption events (TDEs) have been proposed as valuable laboratories for studying dormant black holes. However, progress in this field has been hampered by the limited number of observed events. In this work, we present TDECat, a comprehensive catalogue of 134 confirmed TDEs (131 optical TDEs and three jetted TDEs) discovered up to the end of 2024, accompanied by multi-wavelength photometry (X-ray, UV, optical, and infrared) and publicly available spectra. We also study the statistical properties, spectral classifications, and multi-band variability of these events. Using a Bayesian Blocks algorithm, we determined the duration, rise time (t_{rise}), decay time (t_{decay}), and their ratio for 103 flares in our sample. We find that these timescales follow a log-normal distribution. Furthermore, our spectral analysis shows that most optical TDEs belong to the TDE-H+He class, followed by the TDE-H, TDE-He, and TDE-featureless classes, which is consistent with expectations from main-sequence star disruption. Using archival observations, we identified three new potentially repeating TDEs, namely, AT 2024pvu, AT 2022exr, and AT 2021uvz, increasing the number of known repeating events. In both newly identified and previously known cases, the secondary flares exhibit a similar shape to the primary. We also examined the infrared and X-ray emission from the TDEs in our catalogue, and find that 14 out of the 18 infrared events have associated X-ray emission, strongly suggesting a potential correlation. Finally, we find that for three sub-samples (repeating flares, infrared-emitting events, and X-ray-emitting events), the spectral classes are unlikely to be randomly distributed, suggesting a connection between spectral characteristics and multi-wavelength emission. TDECat enables large-scale population studies across wavelengths and spectral classes, providing essential tools for navigating the data-rich era of upcoming surveys such as the Legacy Survey of Space and Time.

Key words. accretion, accretion disks – black hole physics – methods: statistical – catalogs – galaxies: nuclei

1. Introduction

A tidal disruption event (TDE) occurs when a star ventures too close to a supermassive black hole (SMBH), where differential gravitational forces exceed the star's self-gravity, causing it to be torn apart by tidal forces. This occurs only if the tidal radius, R_T , which is the critical radius within which an object is disrupted by the SMBH, is larger than the event horizon. There is a theoretical upper limit to the SMBH's mass known as the

Hills mass, since $R_T \propto M_{\text{BH}}^{1/3}$. For a solar mass star, this limit is approximately $10^8 M_{\odot}$ (Hills 1975). About half of the stellar material remains bound to the SMBH forming an accretion disc, while the other half is ejected (Rees 1988). This process produces a characteristic flare with a sharp rise in brightness, followed by a gradual decay leading to a plateau. These flares can be observed across the electromagnetic spectrum, from radio to hard X-rays and typically exhibit broad hydrogen and helium lines. The expected detection rate of optical TDEs has been estimated at a few 10^{-5} galaxy⁻¹ yr⁻¹ (Yao et al. 2023), which

* Corresponding author: dlangis@physics.uoc.gr

is at least around one order of magnitude smaller than the theoretically derived rates for TDEs (e.g. Magorrian & Tremaine 1999; Wang & Merritt 2004; Stone & Metzger 2016). Over the past half decade, approximately 10–20 new optical TDEs have been detected annually.

The first TDE was identified during the ROSAT all-sky X-ray survey, with the observed soft X-ray emission attributed to a newly formed accretion disc (Bade et al. 1996; Grupe et al. 1999; Saxton et al. 2020). Since then, numerous TDEs have been detected by various instruments and surveys. In the X-ray band, both XMM-Newton (e.g. Esquej et al. 2007; Lin et al. 2011; Saxton et al. 2019) and eROSITA (e.g. Saxton et al. 2020; Sazonov et al. 2021; Grotova et al. 2025) have observed multiple TDEs and candidates. The Chandra X-ray Observatory and the BAT telescope aboard the Neil Gehrels *Swift* Observatory (Roming et al. 2005; Burrows et al. 2005) have played important roles in follow-up X-ray observations of TDEs discovered at optical wavelengths. Additionally, *Swift*'s UVOT telescope has enabled observations of these events in the ultraviolet.

Optical surveys have significantly contributed to our understanding of TDEs. The All-Sky Automated Survey for Supernovae (ASAS-SN; Shappee et al. 2014; Kochanek et al. 2017; Hart et al. 2023), a global network of small automated telescopes scanning the entire sky for supernovae and other transients, has identified numerous TDEs through their distinctive optical flares (e.g. Holoien et al. 2014, 2016b). Similarly, the Zwicky Transient Facility (ZTF; Graham et al. 2019; Bellm et al. 2019; Masci et al. 2019), with its high-cadence, wide-field survey capabilities, has played a key role in the discovery of optical TDEs (e.g. van Velzen et al. 2021; Hammerstein et al. 2023), by rapidly surveying vast areas of the sky. The Asteroid Terrestrial-impact Last Alert System (ATLAS; Tonry et al. 2018; Heinze et al. 2018; Smith et al. 2020; Shingles et al. 2021) has also been crucial to long-term monitoring of TDEs (e.g. Nicholl et al. 2020; Earl et al. 2025) by providing photometric data in two optical wavebands.

The Gaia photometric Science Alerts system (GSA¹; Hodgkin et al. 2021) has also contributed to TDE discoveries by detecting and providing optical photometry of transient events (e.g. Wevers et al. 2022). Several other surveys were instrumental in early TDE observations, including the Catalina Real-Time Transient Survey (CRTS; Drake et al. 2009), Lincoln Near-Earth Asteroid Research (LINEAR; Stokes et al. 2000), Panoramic Survey Telescope and Rapid Response System (Pan-STARRS; Chambers et al. 2016; Waters et al. 2020; Magnier et al. 2020a,c,b; Flewelling et al. 2020), the Palomar Transient Factory (PTF; Law et al. 2009; Rau et al. 2009; Arcavi et al. 2014) and its successor, the Intermediate Palomar Transient Factory (iPTF²; Hung et al. 2017; Blagorodnova et al. 2017, 2019).

Beyond optical wavelengths, TDEs have been observed in the infrared, initially by the Wide-field Infrared Survey Explorer (WISE; Wright et al. 2010) and later by the Near-Earth Object WISE Reactivation (NEOWISE; Mainzer et al. 2011, 2014; Jiang et al. 2016; Dou et al. 2016). Spectroscopic follow-up observations, including the Sloan Digital Sky Survey (SDSS; York et al. 2000; van Velzen et al. 2011) and the Palomar 200-inch Hale Telescope, have been crucial in classifying TDEs based on their distinctive spectral signatures.

Despite the growing numbers of TDEs no comprehensive catalogue currently exists. Such a resource would enable robust

statistical analyses by providing a dataset large enough to conduct meaningful studies, even if the sample is incomplete. The primary goal of this paper is to compile and present all publicly available photometric and spectroscopic data for confirmed optical TDEs up to the end of 2024. Additionally, we investigate different sub-categories of optical TDEs, including those displaying repeating flares, X-ray outbursts, and IR emission.

Our paper is organised as follows: in Sect. 2, we outline the construction of our main sample of confirmed optical TDEs, along with a sample of TDE candidates. In Sect. 3, we describe the data collection process for the catalogue, while in Sect. 4 we delve into the properties of our sample. Finally, in Sect. 5 we discuss our results and their implications, and we follow it with a summary in Sect. 6.

2. Sample selection

Our sample consists of events identified either in the Transient Name Server (TNS³; 105 sources) or in the literature (29 sources). We differentiate between confirmed TDEs and TDE candidates by organising them into two separate catalogues. The main catalogue consists of TDEs that can be found at least in one optical photometric survey and have an available classification spectrum from the time of the flare. We also include TDEs with featureless spectra (see Sect. 4.2) and the three widely accepted on-axis jetted TDEs from the literature. TDEs that do not meet these criteria are designated as TDE candidates and are included in a separate TDE candidates catalogue.

2.1. Main catalogue

The first step in constructing our sample was to retrieve all objects classified as TDEs from TNS. At the time of this study, TNS listed 98 classified TDEs up to the end of 2024. However, AT 2018meh is the same event as AT 2023clx, so we include only AT 2023clx, reducing the TNS-TDE count to 97. From TNS, we also include 4 additional TDE-H+He events, 3 TDE-He events (see Sect. 4.2 for spectral classification) and a TDE-H+He event that is classified in an AstroNote (AT 2024ule⁴). Hence, our TNS-TDE sample consists of a total of 105 transients.

Beyond TNS, additional TDEs have been identified in various published sample studies. Hammerstein et al. (2023) present a sample of 30 TDEs, observed during the first phase of the ZTF survey (see their Table 1). Of these, 12 are not classified in TNS: AT 2018lni, AT 2018jbv, AT 2019cho, AT 2019mha, AT 2019meg, AT 2020ddv, AT 2020ocn, AT 2020opy, AT 2020mbq, AT 2020qhs, AT 2020riz and AT 2020ysg. We note that this sample includes almost all the TDEs from the sample of van Velzen et al. (2021), except for AT 2019eve. This transient showed spectral and light curve evolution that made its initial TDE classification ambiguous (Hammerstein et al. 2023). For this reason, we opt to include AT 2019eve in Sect. 2.2, where we present strong TDE candidates.

Another TDE sample is presented in Yao et al. (2023) which lists 33 TDEs (see their Table 3). Of these, only three are absent from both the Hammerstein et al. (2023) sample and the TNS-TDE sample, namely, AT 2019baf, AT 2019cmw and AT 2020abri. While these three were classified as TDEs in Yao et al. (2023), there are uncertainties regarding their classification. AT

³ <https://www.wis-tns.org/>

⁴ <https://www.wis-tns.org/astronotes/astronote/2024-318>

¹ <http://gsaweb.ast.cam.ac.uk/alerts>

² <https://www.ptf.caltech.edu/iptf/>

Table 1. Setup of the TDE candidate sample table.

AT name	Alternative names	RA	Dec	Comments	Reference
–	OGLE16aaa	01:07:20.88	–64:16:20.70	TDE candidate in a weak AGN	Wyrzykowski et al. (2017)
AT 2019eve	ZTF19aatylnl/Gaia19bti	11:28:49.650	+15:40:22.30	Persistent H_α line one year post peak	van Velzen et al. (2021), Hammerstein et al. (2023)
AT 2021lwx	ZTF20abrbeie	21:13:48.405	+27:25:50.46	Ultraluminous, long duration transient	Subrayan et al. (2023)
AT 2024kmq	ZTF24aapvieu	12:02:37.273	+35:23:35.22	Luminous, fast, red transient	Ho et al. (2025)
–	Swift J1112+82	11:11:47.32	–82:38:44.20	Likely jetted TDE	Brown et al. (2015)

Notes. We present an example for 5 TDE candidates of how the TDE candidate table is structured. Column 1: TNS name of the TDE candidate; Column 2: alternative name; Columns 3–4: RA and Dec coordinates; Column 5: relevant comments; Column 6: Reference. Full table available at the CDS.

2019baf also appears in Somalwar et al. (2025a) as a TDE, but it lacks a classification spectrum from the time of the flare. Additionally, Somalwar et al. (2025a) cite an unpublished work as the basis for its classification. A similar situation applies to AT 2019cmw, which is also referenced in an unpublished paper in Yao et al. (2023). AT 2020abri, meanwhile, has an optical spectrum taken 395 days after the peak of its optical flare, well after the event had likely faded. Its classification is based on 1) persistent blue colour and lack of cooling, which is inconsistent with the majority of supernovae and 2) the combination of weak H_α emission and strong $H\delta$ absorption, which indicate that the host galaxy is post-starburst (where TDE rates are enhanced; see Sect. 4.3). Since none of these three sources have spectra from the time of their flares, we exclude them from the main sample and place them in the TDE candidates sample.

Additionally, several studies focus on individual TDEs that are neither classified in TNS nor included in large sample studies (e.g. van Velzen et al. 2021; Hammerstein et al. 2023; Yao et al. 2023). We include 17 such sources in our catalogue, with detailed descriptions provided in Appendix A.

In total our main catalogue consists of 134 TDEs (131 optical TDEs and three jetted TDEs), including all confirmed events up to 2024. As it was briefly mentioned in the Introduction, the creation of a catalogue of all the known optical TDEs so far can allow for statistical works, which were previously unable to be carried out due to small sample sizes. We note that this is not a complete sample, since many detected events remain unclassified and certain subtypes (e.g. events detected in IR) are not fully explored.

2.2. TDE candidates

Alongside our main TDE sample, numerous transients have been classified as TDE candidates. These sources are included in a supplementary table, available on our GitHub page (see Sect. 3). We note that this is not an exhaustive list of candidates (e.g. we have not included the IR candidate TDEs from Masterson et al. 2024) and the sources included are not used in any analysis throughout this work. The setup of this file is shown in Table 1. The first four columns list the name and coordinates, while the fifth and sixth columns include remarks on the candidate status and reference studies, respectively. To compile the TDE candidates sample, along with our literature search, we utilised TDEplorer⁵, which is a catalogue of TDEs and candidates identified through natural language processing applied to the abstracts of papers.

⁵ <https://jminding.pythonanywhere.com/main/tdes-by-name>

3. Data

The catalogue is available online on a dedicated GitHub⁶ page. On this page, we have compiled all publicly available photometric and spectroscopic data for the TDEs in our sample. The full catalogue is also available via a local Python-based app. Below we summarise how and from where we collected the photometric and spectroscopic data included in the catalogue. We note that some artifacts could be present in the optical light curves (e.g. see light curve of AT 2019teq) included in the TDECat GitHub page.

3.1. Optical and infrared photometry

For compiling the optical and IR photometric data, we used the Black Hole Target Observation Manager (BHTOM⁷), a web server designed to provide astronomers easy access to astronomical data and a network of telescopes. One of the key features of BHTOM allows the user to compile all the available, archived photometric data in an interactive plot and a .csv downloadable file. The catalogue includes data from several surveys, namely LINEAR, CRTS, ZTF, iPTF, SDSS, ASAS-SN, ATLAS, NEOWISE, Pan-STARRS and GSA.

We also manually searched for CRTS light curves of LSQ12dyw from the Catalina Surveys Data Release 2⁸ (Drake et al. 2009). Furthermore, for specific TDEs, we obtained archival photometric data from previously published studies:

- PS1-10jh: Table S1 in the supplementary information of Gezari et al. (2012).
- ASASSN-15oi: Table A1 of Holoien et al. (2016a).
- AT 2017eqx: Table 1 of Nicholl et al. (2019).
- iPTF16axa: Table A1 of Hung et al. (2017).
- iPTF15af: Table 2 of Blagorodnova et al. (2019).

Since different surveys use different photometric methods, we converted all magnitudes and estimated flux densities in the AB system (Oke & Gunn 1983) throughout this work. The monochromatic AB magnitude is defined as $m_{AB} \approx -2.5 \log(\frac{f_\nu}{3631 \text{ Jy}})$, where f_ν is the spectral flux density and 3631 Jy is the zero point. ZTF magnitudes are calibrated using a source with colour $g - r = 0$ in the AB photometric system. ATLAS, iPTF, Pan-STARRS and ASAS-SN g -band photometry is provided in the AB system. On the contrary, CRTS, ASAS-SN V-band, Swift and NEOWISE⁹ photometry is given in the Vega

⁶ <https://github.com/dlangis/TDECat>

⁷ <https://bhtom.space>

⁸ <http://nessi.cacr.caltech.edu/DataRelease/>

⁹ IR zero points for conversion; https://wise2.ipac.caltech.edu/docs/release/allsky/expsup/sec4_4h.html

system. For Vega-to-AB magnitude conversions, we used the values presented in Table 1 of [Blanton & Roweis \(2007\)](#). The Gaia survey uses an internal calibration different from both the AB and Vega systems.

3.2. X-ray photometry

To study the X-ray emission from TDE sources we used data from *Swift*, *Chandra*, and *XMM-Newton* archives. For each TDE source, we analysed all observations available from these missions, and evaluated X-ray fluxes and spectra for each observation. In addition to *Swift*-XRT, *Chandra*-ACIS and *XMM-Newton*-EPIC data, we searched for X-ray counterparts in the 13th data release of the fourth XMM-Newton serendipitous source catalogue (4XMM-DR13, [Webb et al. 2020](#)) and eROSITA main catalogue (eRASS1, [Merloni et al. 2024](#)). A detailed description of the X-ray data reduction is provided in Appendix B.

3.3. Ultraviolet photometry

To evaluate TDE variability in UV-optical bands, we used data from the Swift Ultraviolet and Optical Telescope (UVOT; [Roming et al. 2005](#)), which provides photometry in three near-UV (UVW2, UVM2 and UVW1) and three optical (U, B, V) bands.

The UVOT data were downloaded from HEASARC¹⁰ and reduced using standard procedures¹¹ (HEASoft package v. 6.33.2). After checking the correct World Coordinate System alignment with USNO-B Catalogue ([Monet et al. 2003](#)), we combined image extensions using UVOTIMSUM and merged exposure maps.

Sources were detected using UVOTDETECT. As with XRT data (see Appendix B.1), we assigned UVOT counterparts based on proximity to the TDE source coordinates: if a UVOT source was detected within 5'', its coordinates were adopted. If no source was detected within 5'', we used the TDE source coordinates.

We performed source photometry using UVOTSOURCE with an aperture radius of 5'' for all filters. The background region was an annulus centred at the source with inner and outer radii of 10'' and 15'', respectively, removing emission from overlapping sources. All magnitudes were corrected for Galactic extinction using reddening estimates from [Schlafly & Finkbeiner \(2011\)](#) and the extinction model from [Fitzpatrick & Massa \(2007\)](#). We note that these data are not host subtracted.

3.4. Spectroscopic data

All optical spectra included in the catalogue were obtained from either TNS or the Weizmann Interactive Supernova Data Repository¹² (WiSeREP; [Yaron & Gal-Yam 2012](#)). Hence, the catalogue does not include optical spectra for TDEs not classified in TNS. For the 12 TDEs from [Hammerstein et al. \(2023\)](#), the classification spectra can be found in their Figs. 2 and 14–16. For AT 2018lni, AT 2019cho, AT 2019mha and AT 2019meg, the classification spectra can be found in [van Velzen et al. \(2021\)](#).

Additionally, in the following we list references for (mainly optical) spectra of 13 TDEs that are not in the TNS-TDE sample or included in a previously published catalogue:

- AT 2023vto: Fig. 4 in [Kumar et al. \(2024\)](#).

¹⁰ <https://heasarc.gsfc.nasa.gov/>

¹¹ <http://www.swift.ac.uk/analysis/uvot/image.php>

¹² <https://www.wiserep.org>

- AT 2022agi: Figs. 2 (optical), 3 (UV) in [Sun et al. \(2024\)](#).
- AT 2017gge: Fig. 2 (optical) in [Wang et al. \(2022\)](#), Fig. 5 (near IR) in [Onori et al. \(2022\)](#).
- AT 2017eqx: Figs. 1, 3 in [Nicholl et al. \(2019\)](#).
- LSQ12dyw^{†13}.
- PTF09djl[†]: Figs. 4, 14 in [Arcavi et al. \(2014\)](#).
- PTF09ge[†]: Fig. 12, 14 in [Arcavi et al. \(2014\)](#).
- PS1-10jh[†]: Fig. 1 in [Gezari et al. \(2012\)](#).
- iPTF15af[†]: Figs. 3 (optical), 4 (UV) in [Blagorodnova et al. \(2019\)](#).
- iPTF16axa[†]: Figs. 7, 8 in [Hung et al. \(2017\)](#).
- ASASSN-14li[†]: Fig. 3 in [Holoien et al. \(2016b\)](#).
- ASASSN-14ae[†]: Figs. 4, 5 in [Holoien et al. \(2014\)](#).
- ASASSN-15oi[†]: Fig. 3 in [Holoien et al. \(2016a\)](#).

4. Exploring the catalogue

After having constructed our main sample, we now explore its various subcategories and interesting objects. Specifically, we present the statistics and spectral classes of the TDEs in the catalogue, along with new results on TDEs with repeating flares, delayed IR emission and X-ray outbursts.

4.1. Catalogue statistics

In this section, we analyse the flaring characteristics of the TDE population, in terms of rise and decay times and the event durations. To achieve this, we applied the Bayesian Blocks ([Scargle 1998](#); [Scargle et al. 2013](#)) algorithm, which partitions a one-dimensional flux time series into blocks, each modelled by a constant flux. To avoid overfitting, we include a user-specified penalty parameter for each additional block.

Given flux measurements $\{f_j\}$ and their uncertainties $\{\sigma_j\}$, we first compute cumulative weighted sums (with $w_j = 1/\sigma_j^2$) up to each index: $\sum w$, $\sum(wf)$, $\sum(wf^2)$. These cumulative sums allow for efficient computation of sums over any sub-interval $[k, i]$ via $\text{Sum}([k, i]) = \text{Cumulative Sum}[i] - \text{Cumulative Sum}[k]$. Consequently, the maximum-likelihood estimate for the constant flux μ in a block spanning $[k, i]$ is $\mu = \frac{\sum_{j=k}^{i-1}(w_j f_j)}{\sum_{j=k}^{i-1} w_j}$.

Assuming Gaussian errors, the log-likelihood of modelling data in the interval $[k, i]$ with a single constant value μ is

$$\log(\mathcal{L}) = -\frac{1}{2} \sum_{j=k}^{i-1} \frac{(f_j - \mu)^2}{\sigma_j^2}. \quad (1)$$

By expanding the summation in the exponent, one obtains $-\frac{1}{2} \left[\sum_{j=k}^{i-1} w_j f_j^2 - 2\mu \sum_{j=k}^{i-1} w_j f_j + \left(\sum_{j=k}^{i-1} w_j \right) \mu^2 \right]$.

Moreover, the algorithm uses dynamic programming to determine the optimal segmentation. For each index i (ranging from 1 to the total number of data points n), all possible previous boundaries k (from 0 to $i - 1$) are considered. We computed

$$\text{candidate_score} = \text{best}[k] + \log(\mathcal{L}_{k \rightarrow i}) - \text{penalty},$$

where

- $\text{best}[k]$ is the optimal (maximum) log-likelihood score obtained for the segmentation of the interval $[0, k]$,
- $\log(\mathcal{L}_{k \rightarrow i})$ is the log-likelihood for modelling the new block $[k, i]$ with constant flux, and

¹³ The [†] symbol indicates the sources that have spectra available in WiSeREP.

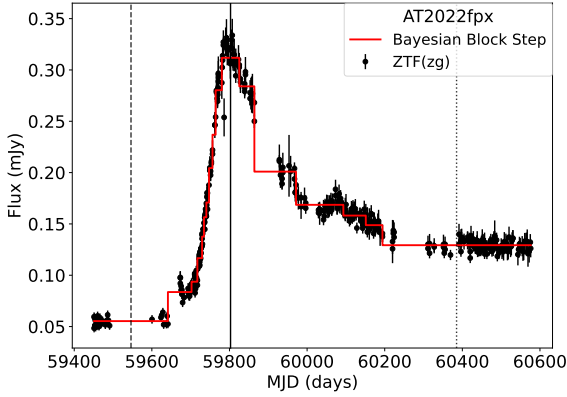


Fig. 1. Example of the implementation of the Bayesian Blocks algorithm to the ZTF light curve of AT 2022fpx. The red solid line shows the optimal blocks and the dashed, dotted and solid black lines represent the rise, decay, and peak times, respectively.

- penalty is a user-specified constant subtracted each time a new block is added. We chose a default value of ten for the penalty to avoid overfitting or underfitting (i.e. small or large penalty values respectively).

The optimal segmentation was obtained by choosing the k that maximises candidate_score followed by a backtracking step (from $i = n$ to 0) to recover the optimal boundaries.

Applying the Bayesian Blocks algorithm to the flux light curves yields blocks within which the flux is assumed to be constant. For each block, we record its mean flux value. The peak of the flare is then identified as the block with the highest mean flux. We primarily use ZTF(zg) light curves (76/103). In case ZTF data are not available or the ZTF(zg) light curve is poorly sampled, we used the light curve with the best sampling. This resulted in 11 ZTF(zr) light curves, six ATLAS light curves, five ASAS-SN light curves, one GSA(G) light curve, one PS1 light curve, one CRTS(CL) light curve, and two PTF light curves.

To estimate the rise and decay times of the flare, we apply a 2.5% amplitude-based threshold (amplitude = peak flux – minimum flux). Starting from the peak block, we move to lower flux levels (to lower or higher block indices) until encountering a block with a mean flux below this threshold. The first sub-threshold block on the left marks the start of the rise, while the first sub-threshold segment on the right marks the end of the decay. From these boundaries, we calculate the rise time, t_{rise} , and decay time, t_{decay} , and determine their ratio $t_{\text{rise}}/t_{\text{decay}}$. We note that in cases where the noise of the data is larger than the 2.5% amplitude-based threshold, the flare is not constrained to when it drops to 2.5%, but where it reaches the observational noise.

An example of this process is displayed in Fig. 1. For this example, the rise time is 256 ± 98 days, the decay time 582 ± 192 days and the peak time $59\,803 \pm 22$ modified Julian date. The duration of the flare, calculated as the sum of the rise and decay times, is roughly 838 days.

We applied this method to 103 TDE flares in our sample, excluding most of the sources detected in 2024 and some older ones where rise or decay times could not be reliably estimated due to large gaps in the light curves. We also included both flares for AT 2022dbl and AT 2020vdq (see Sect. 4.3). Figure 2 shows the distribution of the common logarithm (i.e. logarithm with base 10) of the ratio $t_{\text{rise}}/t_{\text{decay}}$ in our sample. A Kolmogorov-Smirnov (KS) test of the data against a normal distribution with

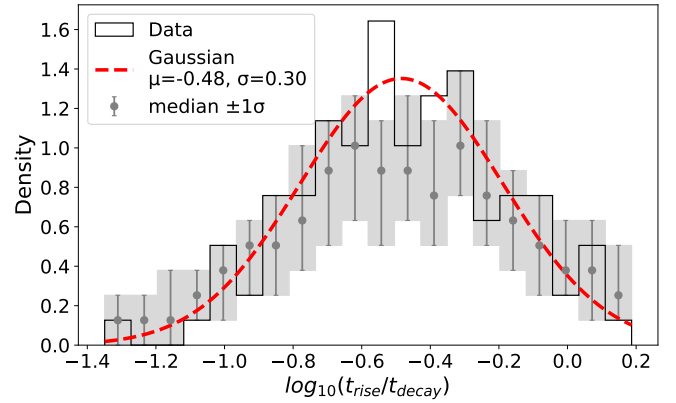


Fig. 2. Distribution of the $t_{\text{rise}}/t_{\text{decay}}$ ratio for 103 TDE flares in our catalogue (black step histogram). The dashed red line indicates a Gaussian distribution with $\mu = -0.48$ and $\sigma = 0.30$ overlotted on the data. The grey data points and boxes represent the median of the mock distributions for each bin and corresponding uncertainty respectively.

$\mu = -0.48$ and $\sigma = 0.30$ (the mean and standard deviation of the data respectively) yields a p-value of 0.99 (KS statistic = 0.04). This means that the $t_{\text{rise}}/t_{\text{decay}}$ ratio distribution is consistent with a log-normal distribution.

Furthermore, we estimated the statistical errors of the histogram in Fig. 2 (and Fig. 3). First, we set a fixed width for the bins of the histogram. Then we computed 10^5 realisations of mock histograms by generating new values from a normal distribution of μ equal to each observed value (black step histogram data) and σ , its corresponding error. This resulted in 10^5 mock histograms, with different bin heights. We computed the median of all the realisations for each bin along with its uncertainty (the distance from the median to the 16th percentile for the lower error and the distance from the 84th percentile to the median for the upper error), plotted as the grey points and grey boxes in Fig. 2 (and Fig. 3).

Figure 3 displays the duration, rise and decay times of the flares. We utilised KS tests against Gaussian distributions with means¹⁴ of $\mu = 400 \pm 30$ days, $\mu = 100 \pm 6$ days and $\mu = 300 \pm 20$ days for the duration, t_{rise} and t_{decay} (the error is the standard error of the mean) and standard deviations of $\sigma = 260$ days, $\sigma = 74$ days and $\sigma = 229$ days respectively (which correspond to the mean and standard deviation of the data). The p-values are 0.87, 0.91 and 0.58 (KS statistic of 0.057, 0.054 and 0.075) for the durations, t_{rise} and t_{decay} respectively, consistent with log-normal distributions. We repeat the same process for the statistical errors of the histograms as presented in Fig. 2 for Fig. 3.

The bottom-right panel of Fig. 3 shows a scatter plot of $\log_{10}(t_{\text{rise}})$ versus $\log_{10}(t_{\text{decay}})$, with error bars calculated as $\sqrt{\sigma_{\text{rise or decay}}^2 + \sigma_{\text{peak}}^2}$, where $\sigma_{\text{rise or decay}}$ is half the width of the rise or decay blocks and σ_{peak} is half the width of the peak block. Given errors in both the independent [$\log_{10}(t_{\text{decay}})$] and dependent [$\log_{10}(t_{\text{rise}})$] variables, we employed the orthogonal distance regression (ODR) to fit a best-fit line while accounting for both uncertainties. The best-fit ODR line is shown as the red solid line in the bottom-right panel of Fig. 3, while the grey contour indicates the 95% confidence interval. It is evident that there is large scatter around the best-fit line, $\log_{10}(t_{\text{rise}}) = \alpha \log_{10}(t_{\text{decay}}) + \beta$,

¹⁴ When back-transforming from log space to linear space, smearing retransformation needs to be applied (Duan 1983).

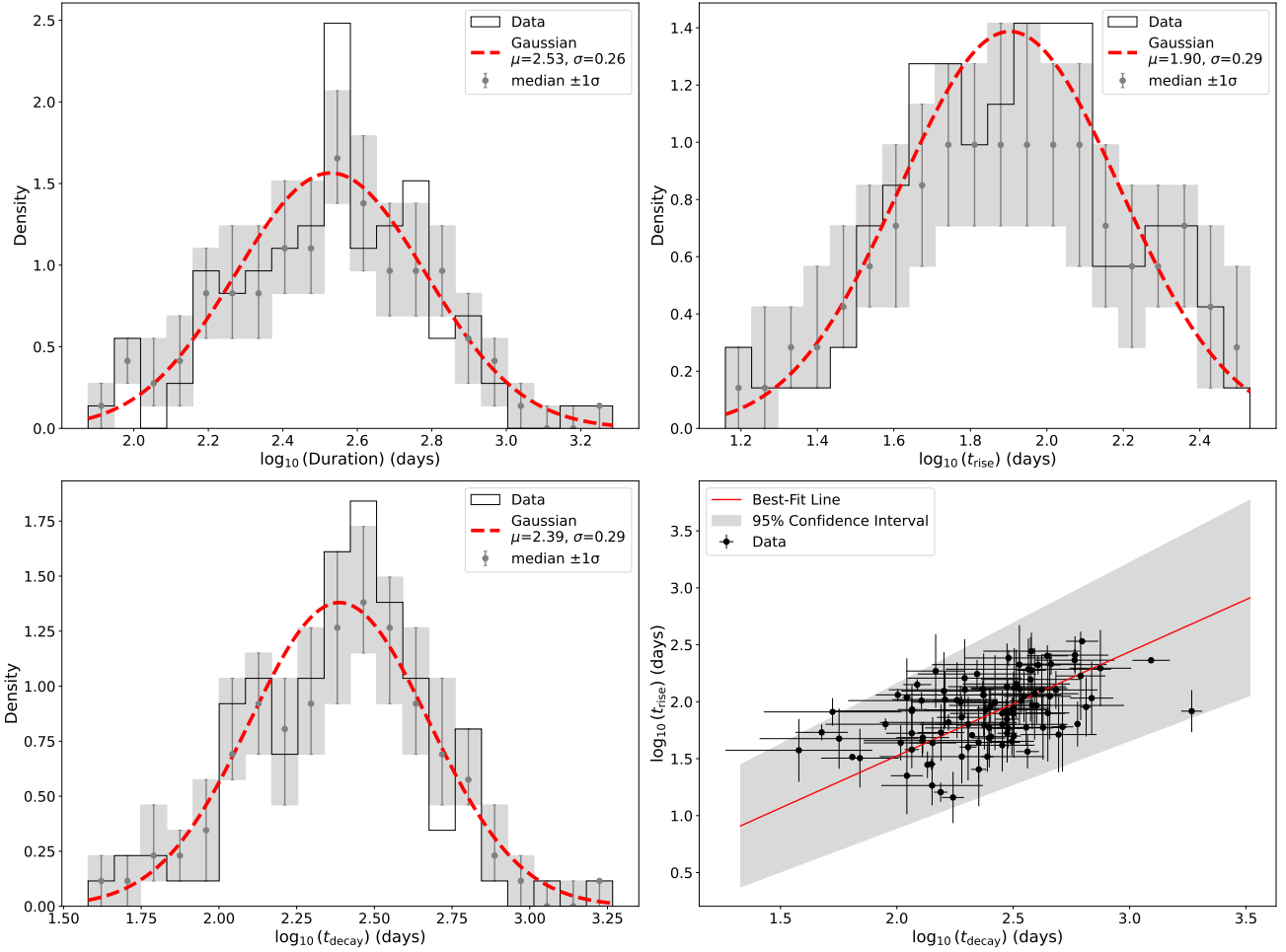


Fig. 3. Distributions of the durations, rise times, and decay times of the flares (top panels and bottom-left panel, respectively), as well as the scatter plot of t_{rise} versus t_{decay} (bottom-right panel). The red dashed lines indicate Gaussian distributions overlotted on the data. The grey data points and boxes represent the median of the generated distributions for each bin and corresponding uncertainty, respectively. In the bottom-right panel the solid red line indicates the best-fit ODR line, while the grey contour represents the 95% confidence interval.

where $\alpha = 0.915 \pm 0.075$ and $\beta = -0.31 \pm 0.17$, with a 95% confidence interval of 0.768 to 1.062 and -0.65 to -0.04 for α and β respectively. We tested whether the correlation between $\log_{10}(t_{\text{rise}})$ and $\log_{10}(t_{\text{decay}})$ is real using a t-test, the Spearman correlation coefficient ($\rho = 0.48$, with a corresponding p-value $\approx 3.6 \times 10^{-7}$), and bootstrapping. In all our tests we could not reject the null hypothesis of a strong, positive correlation between the rise and the decay times.

Figure 4 shows the redshift distributions for the TDEs in the main sample (black step histogram), as well as the optical TDEs (grey step-filled histogram). Both distributions also follow normal distributions in log-space with $\mu = 0.13$, $\sigma = 0.16$ (full sample) equal to the mean and the standard deviation of the data respectively (KS statistic equal to 0.0579 and $p = 0.74$) and $\mu = 0.11$, $\sigma = 0.09$ for the optical TDEs (KS statistic equal to 0.0532 and $p = 0.83$). We discuss further in Sect. 5.1 about potential selection effects that could cause these distribution profiles, along with their use for generating mock data.

Additionally, we used the Anderson-Darling (AD) normality test to further examine the validity of the log-normal behaviour of the timescale and redshift distributions. In all cases, we could not reject the null hypothesis that the distributions are normal (in log-space).

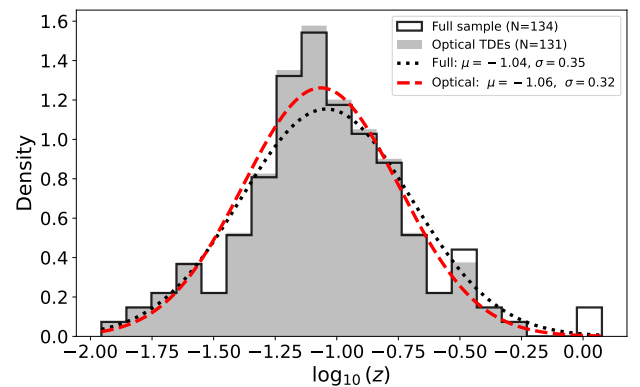


Fig. 4. Distribution of redshift for the TDEs in our sample (black step histogram) as well as the optical TDEs (grey step-filled histogram). The dotted black line indicates a normal distribution overlotted on the full sample, while the dashed red line represents a normal distribution overlotted on the optical TDEs.

4.2. Spectral classification

In this section we investigate the different spectral classes of the TDEs in our sample. For consistency, we adopted the three

spectral classes defined in van Velzen et al. (2021) as well as the TDE-featureless class introduced by Hammerstein et al. (2023):

- TDE-H: in this case, the spectrum exhibits distinct and broad H α and H β emission lines.
- TDE-H+He: here, the spectrum shows both broad H α and H β emission lines and broad He II emission features.
- TDE-He: for this case, the only distinct broad feature in the spectrum appears near the He II emission line with no detectable Balmer emission lines.
- TDE-featureless: here, the spectrum primarily displays host absorption lines with no distinct emission features characteristic of the other three classes.

We note that for most objects in our sample only the classification spectrum is available, typically from the time of the flare. This makes the spectral classification uncertain, as the spectral properties of some TDEs evolve over time (e.g. Charalampopoulos et al. 2022). Several previous studies have already classified the TDEs in their samples, including van Velzen et al. (2021), Hammerstein et al. (2023), and Yao et al. (2023). In some cases, the resulting classifications are mixed. For example, AT 2019mha, AT 2019bhf, and AT 2018hyz appear in two or even all of the above studies, but have different classifications. Additionally, Charalampopoulos et al. (2022) provided spectral classifications for the TDEs in their sample (see their Table 4), some of which contradict the classifications assigned by van Velzen et al. (2021) for overlapping sources (namely ASASSN-15oi and PTF09ge). Furthermore, Charalampopoulos et al. (2022) identified three TDEs: AT 2018hyz, AT 2017eqx and ASASSN-14ae, that show spectral evolution over time (see their Table 4). Throughout this analysis, we assign events to the TDE-H+He class if they have been classified as such in at least one observation epoch. Additionally, six more transients listed in TNS have already been assigned a spectral class (three TDE-H+He and three TDE-He). Moreover, spectral classifications or information on the broadness of the emission lines are available in TNS AstroNotes or classification reports of several TDEs. Finally, since the classification spectra are publicly available for almost all sources in the catalogue, we classify the remaining TDEs in this work.

The results of this analysis are presented in Fig. 5. To summarise, 17.6% (23) of the TDEs belong to the TDE-H class, 12.2% (16) are classified as TDE-He, 60.3% (79) fall into the TDE-H+He class and 9.9% (13) are TDE-featureless. We note that even when considering TDEs with multiple classifications based on spectra from different epochs, the overall distribution of spectral classes remains largely unchanged. If we consider the alternative classifications (PTF09ge→TDE-He, ASASSN-14ae→TDE-H, ASASSN-15oi→TDE-He, AT 2017eqx→TDE-He, AT 2018hyz→TDE-H, AT 2019bhf→TDE-H, AT 2019mha→TDE-H), the aforementioned percentages change to 20.6% (27), 13.7% (18), 55.7% (73) and 9.9% (13) for the TDE-H, TDE-He, TDE-H+He and TDE-featureless classes. The spectral classification of each TDE, along with the corresponding references, can be found on the catalogue GitHub page. We discuss the implications of our results in Sect. 5.2.

4.3. Repeating flares

A few TDEs in our catalogue exhibit repeating flares. These flares may correspond to separate disruption events, where different stars are disrupted each time, or they may result from the partial disruption of the same star. In some cases, the re-brightening could be caused by emission from an accretion disc,

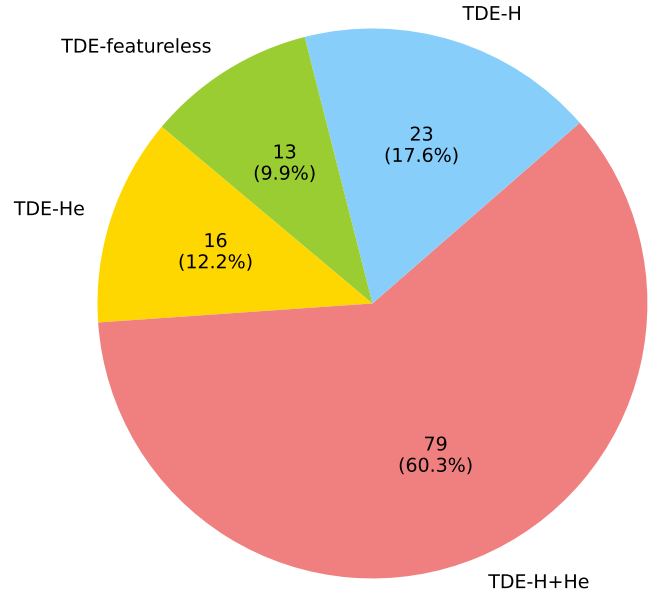


Fig. 5. Percentage of each TDE spectral class in the catalogue.

towards the later stages of the flare. Additionally, AT 2021mhg represents a unique case believed to be a TDE followed by a supernova (SN; Somalwar et al. 2025b). Below, we present our sample of repeating-flare TDEs and our analysis of three previously unreported cases: AT 2024pvu, AT 2022exr, and AT 2021uvz. To the best of our knowledge, these TDEs have not yet been reported as exhibiting a repeating flare.

In total we identified 11 TDEs with multiple flares. The corresponding light curves highlighting the repeating outbursts are shown in Fig. 6. AT 2018fyk is plotted separately in Fig. C.1, since it is the only TDE with Gaia photometry, which cannot be converted to flux. We select the best sampled light curves from the available surveys to maximise the visibility of the flares, plotting only the relevant flare regions.

We approximate the host galaxy emission as the average flux measured prior to the flare. To test the validity of this assumption, we split the light curves into bins corresponding to different ZTF observational seasons for each TDE, compute their average flux and standard deviation and compare the averaged values to the pre-flare flux using a χ^2 test.

In all cases, the reduced χ^2 values and corresponding p-values are consistent with the flux being constant, indicating that the pre-flare light curves can be approximated by the average flux. This average flux is then subtracted from the entire light curve to remove the host galaxy's contribution, retaining only the positive flux variations associated with the transient event. The host-subtracted light curves are displayed in Fig. 6.

The bottom panels of Fig. 6 illustrate the multiple flares of each TDE, overlaid for direct comparison. We normalise the flux to the corresponding flare peak for comparison. We observe that the TDEs in the repeating flare sub-sample display flares that are similar in shape with the confirmed TDE flares. Most notably, we find AT 2024pvu to be the record holder for the longest time separation between two flares (~ 17.9 yr), as well as that AT 2022exr and AT 2021uvz display a double-peak morphology.

For each of the repeating flare TDEs, we examine the possible mechanisms that could explain their multiple flares. We

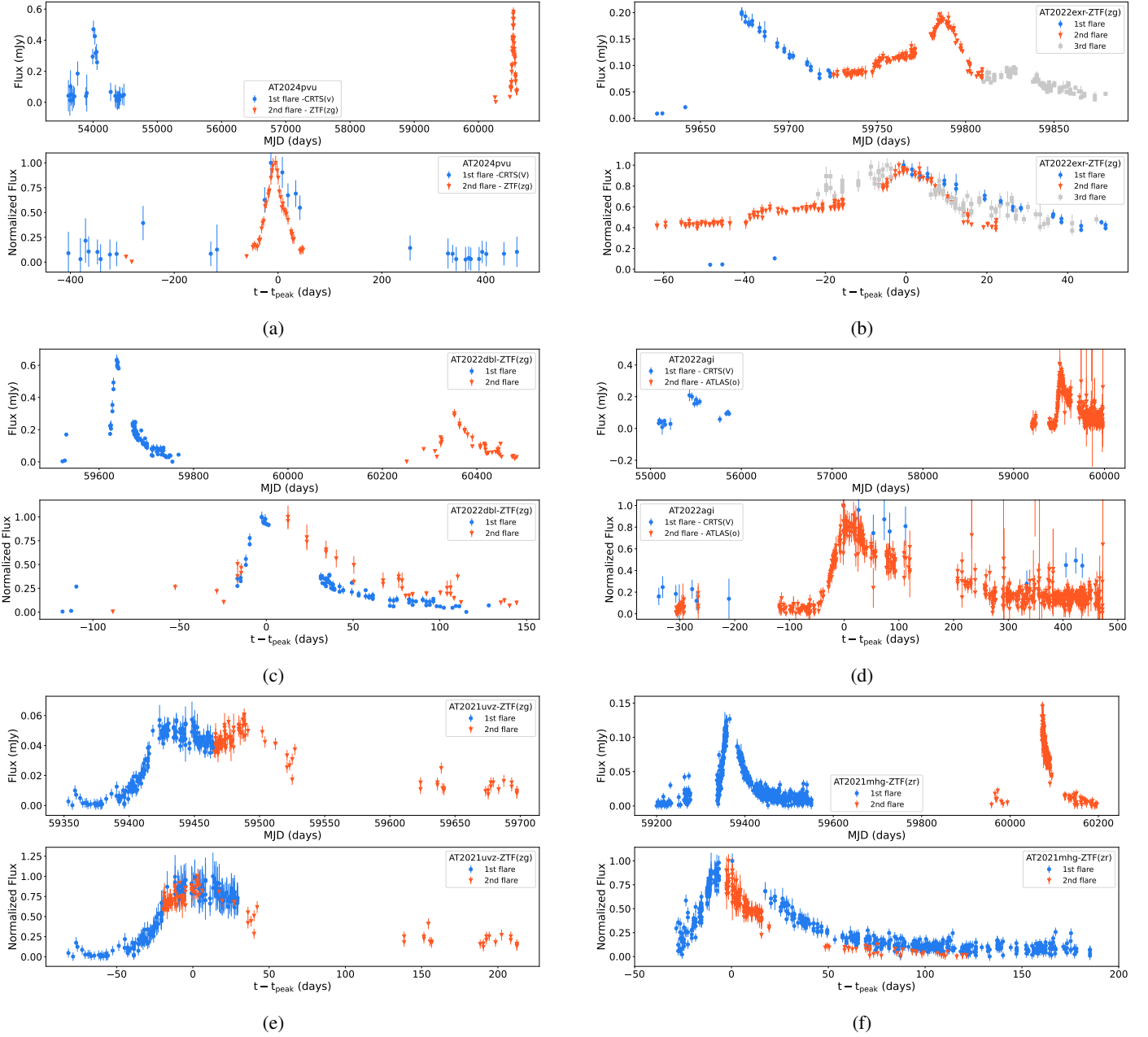


Fig. 6. Optical light curves of the repeating flare TDEs shown in the different panel pairs (a–f). The initial flares are plotted using filled blue circles, with the following flares plotted using filled orange triangles and filled grey squares. In all panel pairs the upper panel shows the optical light curves of the flare regions from different surveys, while the bottom panel displays the two flares, shifted with respect to the flare peak in time and flux.

investigate the repeating partial TDE scenario (pTDE), the disruption of a stellar binary (double TDE) and the disruption of separate, unrelated stars. We also discuss alternative mechanisms for specific cases. A summary of this analysis is presented in Table 2, where the first three columns show the name, the time separation between flares (Δt ; taken from peak to peak) and the number of flares (N_{flare}) respectively, while the final four columns display the different scenarios we considered for the repeating nature of the events ($\checkmark \rightarrow$ likely, $? \rightarrow$ could explain the event but not very probable, $X \rightarrow$ not likely). The relevant references are listed in the final column.

First we explored the separate event scenario for the 11 sources in the repeating flare sample. In order to achieve this, we follow the analysis performed in Sun et al. (2024) for AT

2022agi (IRAS F01004-2237; see their Sect. 5.4). The probability of a separate event occurring in the same host after a time interval of Δt can be computed by $p = r_{TDE} \times \Delta t$, where $r_{TDE} = 3.2^{+0.8}_{-0.6} \times 10^{-5} \text{ yr}^{-1} \text{ galaxy}^{-1}$, which is the incident optical TDE rate from Yao et al. (2023). For each TDE we consider the Δt displayed in the second column of Table 2, whereas the probability for each host galaxy to have another separate event in Δt is given in the parenthesis of the sixth column. We observed that the smallest value is 4.8×10^{-6} , while the largest is 5.7×10^{-4} . For p to exceed > 0.05 , the TDE rate would need to be roughly 87, 152 and 108 times higher for AT 2024pvu, AT 2022agi and AT 2019azh respectively, while for the rest it would need to be 422 times higher or more, reaching $\sim 10\,370$ times for AT 2021uvz. For the first three we list, the required rate could be

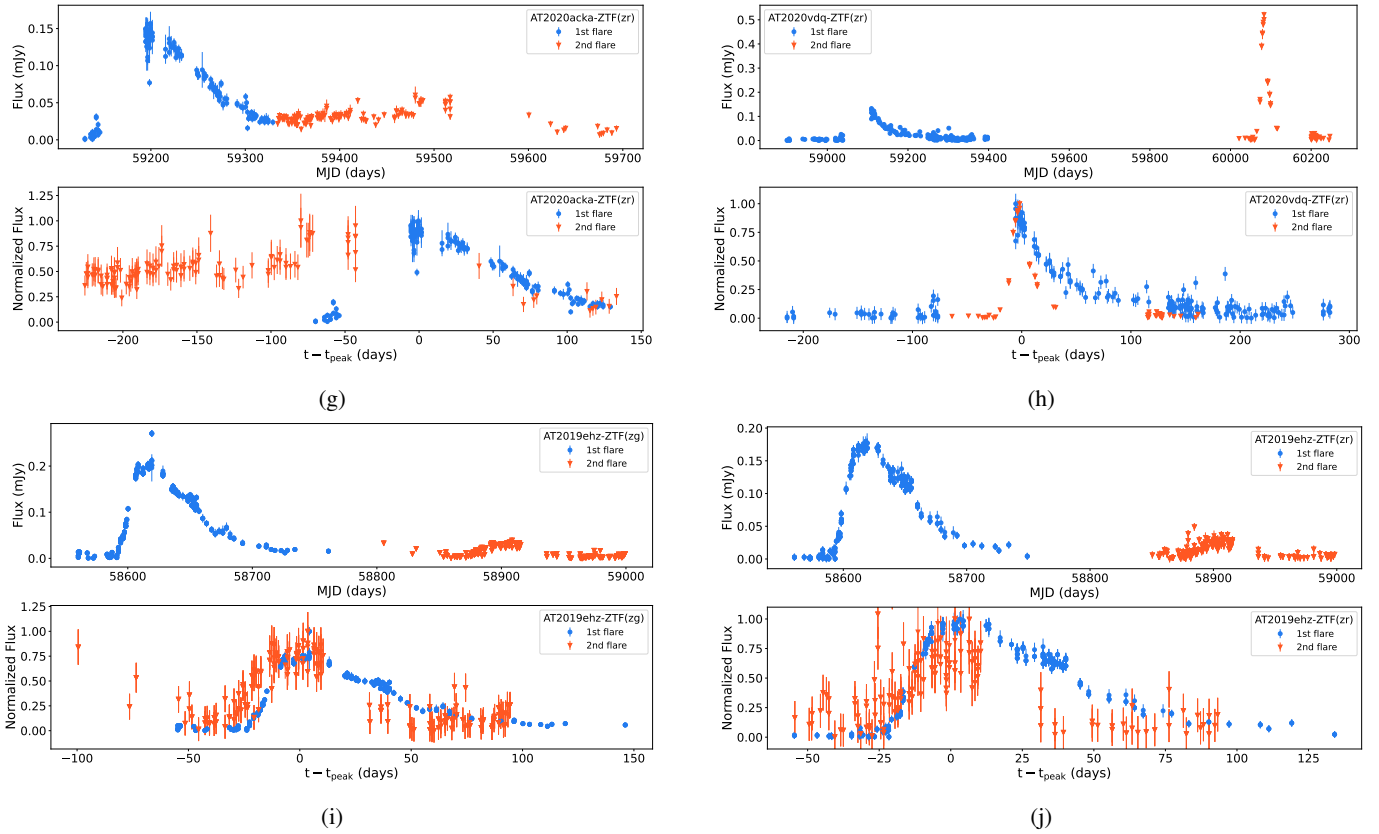


Fig. 6. Continued.

theoretically possible given the enhanced rates in post starburst galaxies, which can have boosted rates of up to ~ 200 times on average (e.g. French et al. 2016; Law-Smith et al. 2017; Graur et al. 2018). However, for the latter cases, we can confidently exclude the scenario that the two flares were caused by separate events, since their rates would need to be enhanced by more than 400 times. We note that the reported p-values do not account for the look-elsewhere effect and could be substantially higher (even by a factor of 100 depending on the event). The correct treatment of the look-elsewhere effect would require dedicated simulations which are beyond the scope of this work.

In order to study whether the multiple flares could be explained by the partial disruption of the same star, we utilised a toy model to calculate the eccentricity. If we assume a solar-like star, a SMBH with a mass of $10^6 M_\odot$ and an orbital period of Δt , we retrieve orbits between the range $1 - e_{max} \approx 0.0007$ and $1 - e_{min} \approx 0.02$. Such orbits would be highly unstable, making the pTDE scenario unlikely. However, such highly eccentric orbits could be explained by the Hills Mechanism (Hills 1988), where the SMBH tidally breaks a stellar binary: one star is ejected with hyper-velocity while the other is captured on an extreme eccentric bound orbit. We use another toy model to qualitatively probe this scenario. Using Eq. (3) of Pfahl (2005, or Eq. (8) of Sun et al. 2024) the semi-major axis of the captured star can be associated with the properties of the binary (the binary semi-major axis, a_b , and the total mass of the binary, $M = M_1 + M_2$). Assuming two solar-like stars and $M_{BH} = 10^6 M_\odot$, we find that using Δt as the observed period yields a_b values that are between $\sim 1.4 R_\star$ to $\sim 33.4 R_\star$. We can access if the two stars are far enough to avoid a common envelope by calculating the effective radius of the Roche lobe, R_{RL} , using Eq. (2) in Eggleton (1983). For two cases, namely AT 2022exr and AT 2021uvz (which

have a double-peaked light curve morphology), we find that this scenario is not plausible, since $R_{RL} > a_b/R_\star$. To further probe the parameter space of the toy model, we use an M_{BH} range $[10^5, 10^8]$ with a step of 0.5 dex, as well as unequal mass and radius stellar binaries. For each case we repeat the above analysis and we also consider only the cases where $R_t > R_{Schwarzschild}$. We find that all the multiple flares could be explained by our toy model in the aforementioned parameter space, and hence we cannot exclude the pTDE scenario for any of them.

An alternative explanation of the repeating flares could be the disruption of a stellar binary (double TDE), which has been studied through simulations (e.g. Mandel & Levin 2015; Mainetti et al. 2016). The difference with the Hills mechanism is that now both stars are disrupted, either in sequence or with a delay, since after the first TDE, the second star is captured in an elliptical orbit around the SMBH. Mandel & Levin (2015) use a population model for the binaries approaching the SMBH with small impact parameters and numerical experiments, which follow Newtonian stellar dynamics of binaries that approach a SMBH. They found that 18% of their simulations yield the subsequent disruption of both stars. As noted by Mandel & Levin (2015), this channel could produce a double-peaked flare similar to the ones observed in AT 2022exr and AT 2021uvz, but they stress that hydrodynamical simulations would be needed to test this hypothesis. Mainetti et al. (2016) modelled light curves of double TDEs using smoothed particle hydrodynamics simulations; however, these simulations did not produce double peaked light curves. Nevertheless they did find a knee¹⁵ in the decay of the simulated light curves in the cases where both stars in an equal-mass binary were partially disrupted or in cases with highly

¹⁵ Noticeable change in the slope of the light curve.

Table 2. Properties of the repeating flare sample.

Name	Δt (days)	N_{flares}	pTDE	Double TDE	Separate events (p)	Other	References
AT 2024pvu	~6535	2	✓	✓	✓ (5.7×10^{-4})	–	i
AT 2022exr	~110 (~35)	3	✓	?	X (9.6×10^{-6})	–	i
AT 2022dbl	~695	2	✓	✓	X (6.1×10^{-5})	–	ii, iii
AT 2022agi	~3760	2	✓	✓	✓ (3.3×10^{-4})	–	iv
AT 2021uvz	~55	2	✓	?	X (4.8×10^{-6})	–	i
AT 2021mhg	~710	2	X	X	X (6.2×10^{-5})	α	v, vi
AT 2020vdq	~995	2	✓	✓	X (8.7×10^{-5})	–	vi, vii, viii
AT 2020acka	~300	2	✓	✓	X (2.6×10^{-5})	β	ix, x
AT 2019azh	~5295	2	✓	✓	✓ (4.6×10^{-4})	–	xi, xii
AT 2019ehz	~300	2	✓	✓	X (2.6×10^{-5})	β	vii, x, xii
AT 2018fyk	~1350	2	✓	✓	X (1.2×10^{-4})	–	xiii, xiv

Notes. Column 1: name of the TDE. Column 2: time separation between the peaks (the parenthesis for AT 2022exr is the time separation between the second and third flares). Column 3: number of flares. Column 4: partial TDE scenario. Column 5: disruption of a stellar binary scenario. Column 6: disruption of separate stars scenario. Column 7: other potential mechanism (α = TDE followed by SN, β = accretion disc fluctuation or a sudden influx of excess orbiting material from the disrupted star). Column 8: references, (i) this work, (ii) Lin et al. (2024), (iii) Makrygianni et al. (2025), (iv) Sun et al. (2024), (v) Munoz-Arancibia et al. (2023), (vi) Somalwar et al. (2025b), (vii) Yao et al. (2023), (viii) Charalampopoulos et al. (2023), (ix) Guo et al. (2025), (x) Zhong (2025), (xi) Hinkle et al. (2021), (xii) Hammerstein et al. (2023), (xiii) Wevers et al. (2019), (xiv) Wevers et al. (2023).

unequal-mass binaries. We observe a knee in the decay of the light curve of AT 2019ehz (see Figs. 6i and 6j), where one of the stars could have been caught in an orbit to explain the second flare ~300 days after the first one. Furthermore, in about 2.5% of their simulations, Mandel & Levin (2015) found that one star would get fully disrupted, while the second was captured in a bound orbit with a period of at least 6 months (and a median period of roughly 50 years). This scenario could explain the double peaked light curves of all the repeating flare TDEs, except AT 2022exr, AT 2021mhg and AT 2021uvz.

There are also additional mechanisms that might be responsible for the multiple flares. One example is AT 2021mhg, where the TDE flare was followed by a SN Type Ia (Somalwar et al. 2025b). Additionally, AT 2019ehz and AT 2020acka display secondary, dimmer flares, which could result from an accretion disc fluctuation or a sudden influx of excess orbiting material from the disrupted star (Guo et al. 2025).

4.4. Multi-wavelength flares

A small subset (18) of optical TDEs in our sample display IR flares, namely, AT 2023ugy, AT 2023cvb, AT 2022upj, AT 2022fpx, AT 2022agi, AT 2022dyt, AT 2022aee, AT 2021uqv, AT 2020afhd, AT 2020ksf, AT 2020mot, AT 2020nov, AT 2020pj, AT 2019qiz, AT 2019dsg, AT 2019azh, AT 2017gge, and ASASSN-14li. In Fig. 7, we show two examples of IR light curves (lower panels) from the NEOWISE survey (W1 and W2 filters), in addition to optical (middle panels) and X-ray data (upper panels). Only four TDEs (i.e. AT 2023ugy, AT 2022aee, AT 2020mot, and AT 2020pj) lack an X-ray counterpart (only upper limits are available).

Following the process described in Sect. 3.3, we retrieved UVOT photometry for 118 TDEs. An example light curve (AT 2020nov) is displayed in Fig. 8. In total, 111 TDEs have data for all six wavebands, while 95 have at least five observations for each of the three UV bands. These data can be accessed through the GitHub page, under the UVOT folder in the photometry section.

We also investigated TDEs observed in X-rays (see Sect. 3.2). In our main sample, 126 sources either have detections or 3σ upper limits in the X-rays. Of these, 45 TDEs have at least one detection, while 26 have at least five detections. Example light curves are shown in the upper panels of Fig. 7. We note that we analyse X-ray observations individually, meaning that stacking observations will lead to more detections. We also consider as detections only the observations with signal-to-noise (S/N) ratio equal to or greater than three. The S/N of the observations is also included in the GitHub files of each source, so the users can set the limit to the threshold they want. All available X-ray, UV and IR data can be found in the accompanying GitHub repository and plotted using the provided app.

5. Discussion

5.1. Statistics of the sample

In Sect. 4.1, we showed that the distributions of the duration, t_{rise} and t_{decay} , as well as their ratio, are consistent with a log-normal distribution. These distributions, along with the scatter plot in the bottom-right panel of Fig. 3, can be used to generate mock TDE data. We note that this is the first time that the timescales in TDEs have been parametrised with a large sample of more than 100 TDEs. Previously, van Velzen et al. (2021) had a final sample of 39 TDEs, for which they inferred their timescales through fitting, and found that there was no correlation between rise times and decay times. However, Hammerstein et al. (2023) and Yao et al. (2023), who studied 30 and 33 TDEs respectively, later reported that there is a positive correlation between rise and decay times, similar to our results (bottom-right panel of Fig. 3).

The log-normal behaviour of the redshift distribution could result from observational selection effects, due to the sensitivity of current telescopes and the local universe galaxy density, rather than from some intrinsic property of TDEs. We expect that the distribution of redshifts will change with the addition of data from upcoming surveys such as the Legacy Survey of Space and Time¹⁶ (LSST; Ivezić et al. 2008). Furthermore, the

¹⁶ <https://www.lsst.org/about>

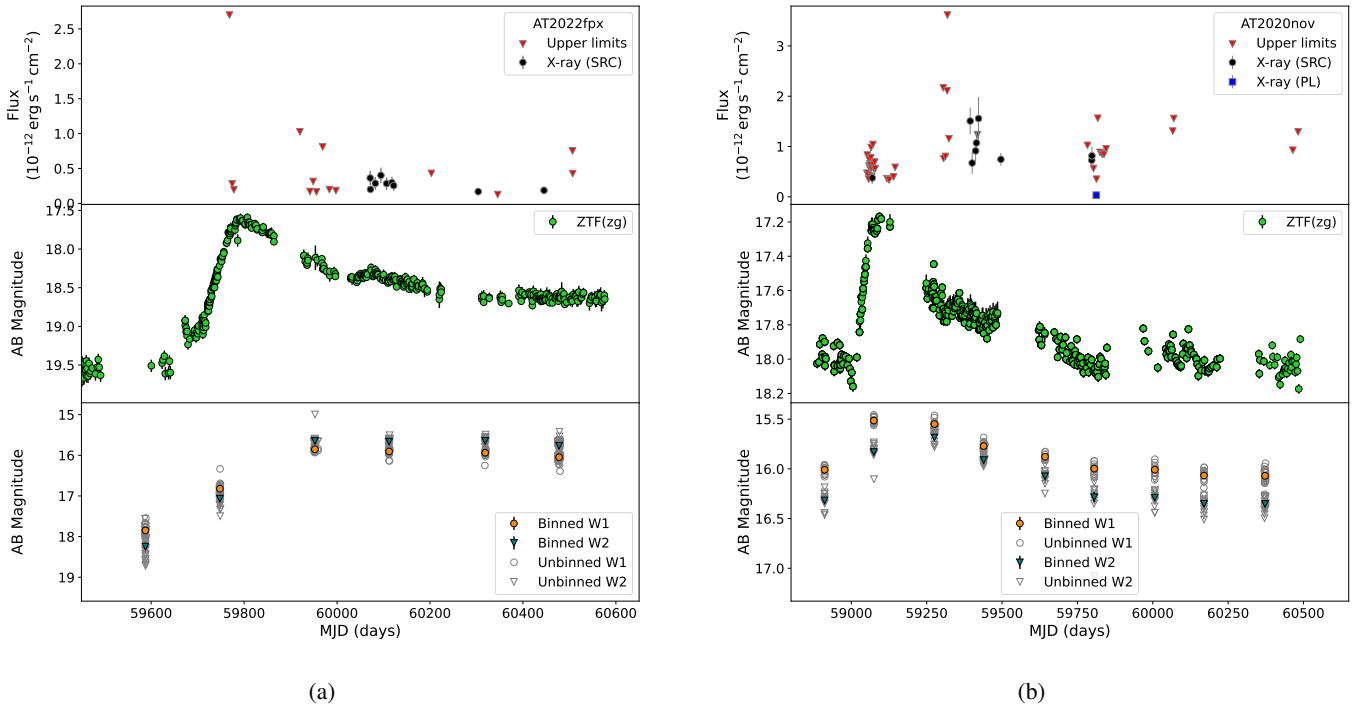


Fig. 7. X-ray, optical, and IR light curves of AT 2022fpx and AT 2020nov in the upper, middle, and bottom panels respectively. For the IR light curves, we show both W1 and W2 binned NEOWISE light curves using orange filled circles and upside-down filled blue triangles respectively, while their un-binned data points are plotted with grey shapes.

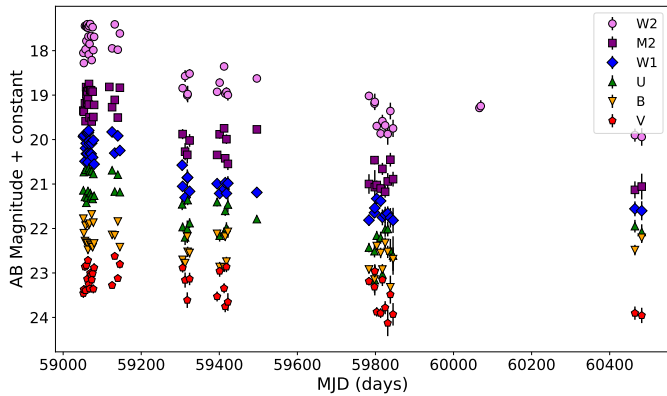


Fig. 8. UVOT light curves for AT 2020nov.

redshift distribution, along with the rest of the distributions from Sect. 4.1, can be used to generate mock TDE populations and light curves.

5.2. Spectral classes

As shown in Fig. 5, the majority of TDEs fall into the TDE-H+He category. As predicted by Syer & Ulmer (1999), the disruption of main-sequence (MS) stars by SMBHs of mass $\lesssim 10^8 M_{\odot}$ would be the easiest for modern-day telescopes to observe. MS stars consist of both hydrogen and helium, hence the observed spectral signatures. Moreover, MS stars are abundant in galactic centres due to their long-lived nature and have been found to dominate TDE rates in past studies (e.g. Kochanek 2016). The second most common spectral class in our sample is TDE-H, followed by TDE-He and TDE-featureless classes. The

statistical study of Nicholl et al. (2022) uncovered that for the TDE-H sources in their sample, their impact parameter (b ; i.e. high $b \rightarrow$ almost full disruption, small $b \rightarrow$ partial disruption) was by far the smallest compared to TDE-H+He and TDE-He, corresponding to partial disruptions. The outer layers of MS stars are mainly hydrogen, so the partial disruption of the outer layers of MS stars could explain the observed TDE-H population. Additionally, hydrogen-rich young MS stars are typically rare, and hence the contribution of their disruption to the population should be small. On the other hand, the TDE-He class is significantly more scarcely observed, with only 16 events (18 if we consider the different epoch classifications from Sect. 4.2). This could be explained by the disruption of helium-rich stellar cores, as suggested by Gezari et al. (2012) for PS1-10jh. These stellar remnants are rare, theorised to be originating from stellar binary systems (e.g. Paczyński 1967; Iben & Tutukov 1985; Götzberg et al. 2019), which could explain their small observed number in TDEs (e.g. Mockler et al. 2024).

Regarding the TDE-featureless class, we have collected data for 13 such events. Hammerstein et al. (2023) found that the 4 TDE-featureless sources in their sample exhibited higher peak bolometric luminosities, hotter temperatures and larger radii than those in the TDE-H and TDE-H+He classes. Moreover, their TDE-featureless sample favoured redder and more massive host galaxies compared to other classes. This trend can be further tested using the TDEs in our catalogue. Additionally, the Hammerstein et al. (2023) featureless TDEs were found in relatively higher redshifts than the rest of their sample. Similarly, we find that 7 of our 13 featureless TDEs display redshifts that are 0.25 or above, where the mean is around 0.1 (median around 0.09). In our sample, $z = 0.25$ is at the 91.6th percentile for the optical TDEs (grey filled histogram from Fig. 4), meaning that 8.4% of the optical TDEs have $z \geq 0.25$. Featureless TDE spectra can arise for several reasons. One possibility is that the

line-emitting regions are obscured, depending on our viewing angle. Another explanation is that dense, optically thick outflows reprocess and thermalise high-energy photons, effectively ‘washing out’ sharp emission lines. Additionally, a strong, hot continuum can overpower weaker lines, making them difficult to detect.

To analyse the variability properties of different spectral classes, we applied the same statistical approach used in Sect. 4.1 to the TDEs for which we could reliably measure flare variability. We then utilised a KS test to assess whether the distributions of different spectral classes are consistent with that of the full sample. We obtained p-values ranging from 0.15 to 0.97 for the rise times, decay times and durations. Although the sample sizes for TDE-H, TDE-He and TDE-featureless classes are small, we find that the timescale distributions of all spectral classes are drawn from the same parent population. [van Velzen et al. \(2021\)](#) had reported that the rise times of their H+He TDEs were longer than the ones for the TDE-H and TDE-He sources. However, this could be due to their smaller sample size along with the small errors from their light curve fitting parameters.

Additionally, we investigated the spectral classes of TDEs in different sub-samples showing either IR emission, repeating flares or X-ray emission. For the IR sample we find that 12 are TDE-H+He, 5 are TDE-H and 1 is TDE-He. For the repeating flare sample we find that 7 are TDE-H+He, 2 are TDE-H and 2 are TDE-featureless. Finally, for the X-ray detection sample we find that 4 are TDE-He, 26 are TDE-H+He, 9 are TDE-H and 3 are TDE-featureless. We estimated the probability that the spectral classes of the different sub-samples are randomly drawn from the full sample using

$$\begin{aligned} \mathcal{P}_{IR} &= \frac{C_{74}^{12} C_{23}^5 C_{13}^1 C_{12}^0}{C_{123}^{18}} \approx 5.9 \times 10^{-3}, \\ \mathcal{P}_{Repeating} &= \frac{C_{79}^7 C_{23}^2 C_{16}^0 C_{13}^2}{C_{134}^{11}} \approx 0.01, \\ \mathcal{P}_{X-ray} &= \frac{C_{74}^{26} C_{23}^9 C_{13}^4 C_{12}^3}{C_{122}^{42}} \approx 8 \times 10^{-3} \end{aligned} \quad (2)$$

where C_n^k is the binomial coefficient. Here, the numerator represents the number of ways to compose a sample with the different spectral classes in each sub-sample while the denominator accounts for all possible selections from the full set of 134 TDEs for the repeating flare sample and 123 TDEs for the X-ray and IR samples¹⁷. The small p-values in all three cases indicate the spectral composition of these sub-samples is unlikely to be random. This could indicate that the spectral characteristics of TDEs are related to their overall multi-wavelength behaviour.

5.3. Similarities and specific cases in the repeating flare sample

From our main catalogue, 11 TDEs exhibit more than one flare. While six of these TDEs have been extensively studied in previous works, two of the remaining five sources (AT 2020acka, and AT 2019ehz) have appeared in past sample studies ([van Velzen et al. 2021](#); [Hammerstein et al. 2023](#); [Yao et al. 2023](#)) without their repeating nature being highlighted. Only recently were AT 2020acka’s and AT 2019ehz’s re-brightening features referenced

¹⁷ 126 TDEs have at least X-ray upper limits; however three of them are jetted TDEs with no optical spectrum available; that is why $k = 42$ in the denominator for the X-ray calculation.

by [Guo et al. \(2025\)](#) and [Zhong \(2025\)](#). Unfortunately, due to a lack of spectroscopic data, we cannot confirm the TDE nature of the flares in the latter half of our repeating flare sample. However, by comparing the rise times, decay times and durations of both flares we find that the timescales for AT 2022dbl, AT 2022agi, AT 2020vdq, AT 2019ehz, and AT 2019azh, are consistent within uncertainty with one another (see Appendix D). We are unable to compute the rise time of the second flare of AT 2021mhg due to substantial gaps in the respective light curve. Additionally, for AT 2022exr and AT 2021uvz, which are the double peak flares, as well as AT 2020acka, we cannot evaluate the shape of their flares since they are overlapping. From a visual inspection, the rise time of the second flare of AT 2021mhg is clearly different and has been identified as a Type Ia SN. Moreover, the flares in AT 2020acka, possibly originating from accretion disc emission, also displays dissimilar shapes. The similarity of the repeating flares has also been previously noted by [Makrygianni et al. \(2025\)](#) for AT 2022dbl and [Hinkle et al. \(2021\)](#) for AT 2019azh.

If the additional flares arise from pTDEs, one could expect their shapes to be similar since they would result from the disruption of the same star (simulation papers that have modelled repeating pTDEs have yet to constrain rise times and decay times; e.g. [Liu et al. 2025](#)). However, the observed diversity in flare shapes suggests that underlying mechanisms may be at play: some flares could indeed be repeating pTDEs, while others may result from distinct events such as double TDEs or unrelated transient phenomena. Moreover, [Liu et al. \(2025\)](#) found in their simulations that a sun-like star would produce multiple flares of increasing luminosity, consistent with AT 2020vdq, whose second flare is more luminous than the first. However, this picture is not consistent with AT 2022dbl (e.g. [Makrygianni et al. 2025](#)), where the opposite behaviour is observed.

Furthermore, seven out of the 11 sources in our repeating flare sample exhibit X-ray detections with the exception of AT 2024pvu, AT 2022dbl, AT 2021mhg, and AT 2020acka, for which we obtained only upper limits. We observe that in some TDEs (AT 2022exr, AT 2020vdq, AT 2019ehz, and AT 2018fyk), the X-ray emission follows the optical flare with only a short delay. In contrast, others (AT 2021uvz, AT 2022agi, and AT 2019azh) display significantly longer delays. Notably, for AT 2022exr and AT 2020vdq, X-rays are detected only after the second flare, while for AT 2018fyk they occur nearly simultaneously with the optical outbursts.

5.4. Possible correlation between X-ray and infrared emission

As shown in Sect. 4.4, most TDEs exhibiting IR flares also display X-ray detections. In fact, 14 out of the 18 IR-flaring TDEs have been detected in X-rays. Moreover, in the sample of IR-selected TDEs from the eROSITA sky presented by [Masterson et al. \(2024\)](#), three of the eight objects (all from their gold sample) were detected in the X-rays at multiple epochs. These findings suggest a potential underlying correlation between IR and X-ray emission.

Notably, both confirmed TDEs associated with astrophysical neutrinos, AT 2019dsg ([Stein et al. 2021](#)) and AT 2017gge ([Li et al. 2024](#)), are included in our IR flare sample. It has been proposed that neutrino production in these events could be linked to radio emission ([Stein et al. 2021](#)), IR emission ([Yuan et al. 2024](#)), or X-ray emission ([Li et al. 2024](#)). However, further study is needed to clarify the association between neutrinos and TDEs, as well as the particle acceleration mechanisms that might lead to neutrino production.

We also investigated whether any sources exhibited delayed IR or X-ray emission relative to their optical flares. Our analysis reveals that in two TDEs (AT 2021uqv, AT 2019dsg) only the IR emission is delayed; in another five cases (AT 2022fpx, AT 2020ksf, AT 2020nov, AT 2020afhd, AT 2019azh), only the X-rays are delayed; and in five cases, both IR and X-ray emissions are delayed, with IR flares generally lasting longer, and the X-ray emission being more delayed. In contrast, for AT 2022dyt and ASASSN-14li, the X-ray and IR emission occur almost simultaneously with the optical flare.

Further similarities emerge within our sample. For example, AT 2022fpx, extensively studied by Koljonen et al. (2024), displays a light curve similar to that of AT 2020nov, where the X-ray emission coincides with a bump in the optical light curve. Furthermore, all coronal line-emitting TDEs, namely, AT 2022fpx (Koljonen et al. 2024), AT 2022upj (Newsome et al. 2022, 2024), AT 2019qiz (Short et al. 2023), and AT 2017gge (Onori et al. 2022), exhibit both X-ray and IR emission.

The statistical significance of the correlation between IR and X-ray emission in our sample of optical TDEs can be estimated by considering a binomial calculation. The chance that a TDE has X-ray emission can be calculated as the detection fraction of the X-rays in our optical TDE sample (i.e. $p=45/126=0.357$). We could therefore test the null hypothesis (i.e. that each of the IR-flaring TDEs has an independent chance $p=0.357$ of X-ray detection) by computing the probability of seeing $k \geq 14$ X-ray detections by chance:

$$P = \sum_{k=14}^{18} \binom{18}{k} p^k (1-p)^{18-k} \approx 3.3 \times 10^{-4} \quad (3)$$

Since $P \ll 0.05$, we reject the null hypothesis, meaning that the observed correlation of X-ray and IR emission in our IR-emitting optical TDE sample is likely not by chance. We can also convert the probability to sigma levels for a one-tailed normal distribution, which gives a 3.4σ significance. We note that this analysis could be biased towards lower redshift sources, that are brighter and more easily observed by modern day telescopes.

6. Conclusions

We have compiled a catalogue of 134 confirmed TDEs up until the end of 2024. We collected multi-wavelength photometry (X-ray, UV, optical, and IR) along with publicly available spectra. The complete dataset is accessible via a dedicated GitHub repository and a Python application. Additionally, we created a list of strong TDE candidates.

We analysed the sources in our main sample by investigating their statistical properties, spectral classes, and the presence of repeating flares, IR emission, and X-ray outbursts. Our key findings are as follows:

1. By implementing a custom Bayesian Blocks algorithm, we estimated the duration, rise time, decay time, and their ratio for the optical flares of 101 TDEs in our sample. A total of 103 flares were analysed, including all flares from repeating pTDEs (AT 2022dbl and AT 2020vdq). We find that the distributions of the t_{rise}/t_{decay} ratio, durations, rise times, and decay times are well described by a log-normal distribution.
2. The best-fit line for $\log_{10}(t_{rise})$ versus $\log_{10}(t_{decay})$ is given by $\log_{10}(t_{rise}) = \alpha \log_{10}(t_{decay}) + \beta$, where $\alpha = 0.915 \pm 0.075$ and $\beta = -0.31 \pm 0.17$, with 95% confidence intervals of 0.768 to 1.062 and -0.65 to -0.04 for α and β respectively. This result indicates that the majority of the TDE population is confined

within the scatter of this best-fit line. We also find a positive correlation between $\log_{10}(t_{rise})$ and $\log_{10}(t_{decay})$. These results, in combination with the log-normal distributions of the timescales, can be used to create artificial light curves for future statistical studies.

3. Our spectral analysis revealed that the majority of TDEs belong to the TDE-H+He class, followed by the TDE-H class, with the TDE-He and TDE-featureless occurring at slightly lower frequencies. This distribution is consistent with expectations based on the predominance of main-sequence stars in galactic centres. Although we computed timescale statistics for the different spectral classes, we did not identify any definite trends.
4. We examined whether specific spectral classes tend to exhibit repeating flares, IR emission, or X-ray outbursts. Our analysis revealed that the spectral class distribution within these TDE sub-samples is unlikely to have arisen by random chance.
5. We identified three new TDEs that show secondary flares in their optical light curves: AT 2024pvu, AT 2022exr, and AT 2021uvz. We further studied recently referenced TDEs displaying re-brightenings: AT 2020acka, and AT 2019ehz. We also compared the shape of the multiple flares for each TDE and found that their shapes are generally similar, excluding AT 2021mhg and AT 2020acka, which exhibit distinct differences.
6. We observed a potential correlation between IR and X-ray emission. Most TDEs (14 out of 18) displaying IR flares also exhibit X-ray detections. We plan to explore this finding further in a future study. Moreover, all reported coronal line emitting TDEs were found to exhibit both X-ray and IR emission.

This comprehensive (mostly optical) TDE catalogue not only provides a robust dataset for statistical studies and machine learning applications but also paves the way for future population studies aimed at understanding the characteristics of still poorly understood TDEs, such as X-ray TDEs (Auchetti et al. 2017; Sazonov et al. 2021; Khorunzhev et al. 2022) and IR TDEs (Jiang et al. 2021; Panagiotou et al. 2023; Masterson et al. 2024). As we enter into the ‘data-rich era’ – especially with forthcoming surveys such as LSST, which are expected to capture tens of TDEs each night – this work serves as an essential tool for preparing for the challenges and opportunities ahead.

Data availability

Table 1 and the catalogue are available at the CDS via <https://cdsarc.cds.unistra.fr/viz-bin/cat/J/A+A/707/A171>. The data and python application (see Sect. 3), along with the aforementioned table information and overall catalogue, can be accessed through the TDECat GitHub repository¹⁸.

Acknowledgements. The authors thank the anonymous referee for comments and suggestions that helped improve this work. DAL, AP, and IL were funded by the European Union ERC-2022-STG – BOOTES – 101076343. Views and opinions expressed are however those of the authors only and do not necessarily reflect those of the European Union or the European Research Council Executive Agency. Neither the European Union nor the granting authority can be held responsible for them. KIIK has received funding from the European Research Council (ERC) under the European Union’s Horizon 2020 research and innovation programme (grant agreement No. 101002352, PI: M. Linares). NG acknowledges support by a grant from the Simons Foundation (00001470, NG). JD, DM, and ZT took part in this research under the auspices of the Science

¹⁸ <https://github.com/dlangis/TDECat>

Internship Program at the University of California Santa Cruz. NG is grateful to Caitlyn Nojiri and Hannah Dykaar for their help. BHTOM has been based on the open-source TOM Toolkit by LCO and has been developed with funding from the European Union's Horizon 2020 and Horizon Europe research and innovation programmes under grant agreements No. 101004719 (OPTICON-RadioNet Pilot, ORP) and No. 101131928 (ACME). We acknowledge ESA Gaia, DPAC and the Photometric Science Alerts Team (<http://gsaweb.ast.cam.ac.uk/alerts>). This work has made use of data from the Asteroid Terrestrial-impact Last Alert System (ATLAS) project. The Asteroid Terrestrial-impact Last Alert System (ATLAS) project is primarily funded to search for near earth asteroids through NASA grants NN12AR55G, 80NSSC18K0284, and 80NSSC18K1575; byproducts of the NEO search include images and catalogues from the survey area. This work was partially funded by Kepler/K2 grant J1944/80NSSC19K0112 and HST GO-15889, and STFC grants ST/T000198/1 and ST/S006109/1. The ATLAS science products have been made possible through the contributions of the University of Hawaii Institute for Astronomy, the Queen's University Belfast, the Space Telescope Science Institute, the South African Astronomical Observatory, and The Millennium Institute of Astrophysics (MAS), Chile. The Pan-STARRS1 Surveys (PS1) and the PS1 public science archive have been made possible through contributions by the Institute for Astronomy, the University of Hawaii, the Pan-STARRS Project Office, the Max-Planck Society and its participating institutes, the Max Planck Institute for Astronomy, Heidelberg and the Max Planck Institute for Extraterrestrial Physics, Garching, The Johns Hopkins University, Durham University, the University of Edinburgh, the Queen's University Belfast, the Harvard-Smithsonian Center for Astrophysics, the Las Cumbres Observatory Global Telescope Network Incorporated, the National Central University of Taiwan, the Space Telescope Science Institute, the National Aeronautics and Space Administration under Grant No. NNX08AR22G issued through the Planetary Science Division of the NASA Science Mission Directorate, the National Science Foundation Grant No. AST-1238877, the University of Maryland, Eotvos Lorand University (ELTE), the Los Alamos National Laboratory, and the Gordon and Betty Moore Foundation. The CSS survey is funded by the National Aeronautics and Space Administration under Grant No. NNG05GF22G issued through the Science Mission Directorate Near-Earth Objects Observations Program. The CRTS survey is supported by the U.S. National Science Foundation under grants AST-0909182. This publication makes use of data products from NEOWISE, which is a project of the Jet Propulsion Laboratory/California Institute of Technology, funded by the National Aeronautics and Space Administration. This publication makes use of data products from the Wide-field Infrared Survey Explorer, which is a joint project of the University of California, Los Angeles, and the Jet Propulsion Laboratory/California Institute of Technology, funded by the National Aeronautics and Space Administration. This work utilises Matplotlib (Hunter 2007), NumPy (Harris et al. 2020) and SciPy (Virtanen et al. 2020).

References

- Alexander, K. D., Berger, E., Guillochon, J., Zauderer, B. A., & Williams, P. K. G. 2016, *ApJ*, **819**, L25
- Alexander, K. D., Velzen, S. V., Miller-Jones, J., et al. 2021, *Transient Name Server AstroNote*, **24**, 1
- Andreoni, I., Coughlin, M. W., Perley, D. A., et al. 2022, *Nature*, **612**, 430
- Arcavi, I., Gal-Yam, A., Sullivan, M., et al. 2014, *ApJ*, **793**, 38
- Auchettl, K., Guillochon, J., & Ramirez-Ruiz, E. 2017, *ApJ*, **838**, 149
- Bade, N., Komossa, S., & Dahlem, M. 1996, *A&A*, **309**, L35
- Bellm, E. C., Kulkarni, S. R., Graham, M. J., et al. 2019, *PASP*, **131**, 018002
- Blagorodnova, N., Gezari, S., Hung, T., et al. 2017, *ApJ*, **844**, 46
- Blagorodnova, N., Cenko, S. B., Kulkarni, S. R., et al. 2019, *ApJ*, **873**, 92
- Blanton, M. R., & Roweis, S. 2007, *AJ*, **133**, 734
- Bloom, J. S., Giannios, D., Metzger, B. D., et al. 2011, *Science*, **333**, 203
- Brimacombe, J., Brown, J. S., Holoien, T. W. S., et al. 2015, *ATel*, **7910**, 1
- Brown, G. C., Levan, A. J., Stanway, E. R., et al. 2015, *MNRAS*, **452**, 4297
- Burrows, D. N., Hill, J. E., Nousek, J. A., et al. 2005, *Space Sci. Rev.*, **120**, 165
- Burrows, D. N., Kennea, J. A., Ghisellini, G., et al. 2011, *Nature*, **476**, 421
- Capalbi, M., Perri, M., Saija, B., Tamburelli, F., & Angelini, L. 2005, *Version*, **1**, 28
- Cenko, S. B., Krimm, H. A., Horesh, A., et al. 2012, *ApJ*, **753**, 77
- Cenko, S. B., Cucchiara, A., Roth, N., et al. 2016, *ApJ*, **818**, L32
- Chambers, K. C., Magnier, E. A., Metcalfe, N., et al. 2016, arXiv e-prints [arXiv:1612.05560]
- Charalampopoulos, P., Leloudas, G., Malesani, D. B., et al. 2022, *A&A*, **659**, A34
- Charalampopoulos, P., Leloudas, G., Pursiainen, M., & Kotak, R. 2023, *Transient Name Server AstroNote*, **115**, 1
- D'Elia, V., Perri, M., Puccetti, S., et al. 2013, *A&A*, **551**, A142
- Dou, L., Wang, T.-g., Jiang, N., et al. 2016, *ApJ*, **832**, 188
- Drake, A. J., Djorgovski, S. G., Mahabal, A., et al. 2009, *ApJ*, **696**, 870
- Duan, N. 1983, *J. Am. Statist. Assoc.*, **78**, 605
- Earl, N., French, K. D., Ramirez-Ruiz, E., et al. 2025, *ApJ*, **983**, 28
- Eggleton, P. P. 1983, *ApJ*, **268**, 368
- Esquej, P., Saxton, R. D., Freyberg, M. J., et al. 2007, *A&A*, **462**, L49
- Fitzpatrick, E. L., & Massa, D. 2007, *ApJ*, **663**, 320
- Flewelling, H. A., Magnier, E. A., Chambers, K. C., et al. 2020, *ApJS*, **251**, 7
- Freeman, P., Doe, S., & Siemiginowska, A. 2001, *SPIE Conf. Ser.*, **4477**, 76
- French, K. D., Arcavi, I., & Zabludoff, A. 2016, *ApJ*, **818**, L21
- Fruscione, A., McDowell, J. C., Allen, G. E., et al. 2006, *SPIE Conf. Ser.*, **6270**, 62701V
- Gehrels, N. 1986, *ApJ*, **303**, 336
- Gezari, S., Chornock, R., Rest, A., et al. 2012, *Nature*, **485**, 217
- Gilfanov, M., Sazonov, S., Sunyaev, R., et al. 2020, *ATel*, **14246**, 1
- Göteborg, Y., de Mink, S. E., Groh, J. H., Leitherer, C., & Norman, C. 2019, *A&A*, **629**, A134
- Graham, M. J., Kulkarni, S. R., Bellm, E. C., et al. 2019, *PASP*, **131**, 078001
- Graur, O., French, K. D., Zahid, H. J., et al. 2018, *ApJ*, **853**, 39
- Grotova, I., Rau, A., Baldini, P., et al. 2025, *A&A*, **697**, A159
- Grupe, D., Thomas, H. C., & Leighly, K. M. 1999, *A&A*, **350**, L31
- Guo, H., Sun, J., Li, S., et al. 2025, *ApJ*, **979**, 235
- Hammerstein, E., van Velzen, S., Gezari, S., et al. 2023, *ApJ*, **942**, 9
- Harris, C. R., Millman, K. J., Van Der Walt, S. J., et al. 2020, *Nature*, **585**, 357
- Hart, K., Shappee, B. J., Hey, D., et al. 2023, arXiv e-prints [arXiv:2304.03791]
- Heizel, A. N., Tonry, J. L., Denneau, L., et al. 2018, *AJ*, **156**, 241
- Hills, J. G. 1975, *Nature*, **254**, 295
- Hills, J. G. 1988, *Nature*, **331**, 687
- Hinkle, J. T., Holoien, T. W. S., Auchettl, K., et al. 2021, *MNRAS*, **500**, 1673
- Ho, A. Y. Q., Yao, Y., Matsumoto, T., et al. 2025, *ApJ*, **989**, 54
- Hodgkin, S. T., Harrison, D. L., Breedt, E., et al. 2021, *A&A*, **652**, A76
- Holoien, T. W. S., Prieto, J. L., Bersier, D., et al. 2014, *MNRAS*, **445**, 3263
- Holoien, T. W. S., Kochanek, C. S., Prieto, J. L., et al. 2016a, *MNRAS*, **463**, 3813
- Holoien, T. W. S., Kochanek, C. S., Prieto, J. L., et al. 2016b, *MNRAS*, **455**, 2918
- Hung, T., Gezari, S., Blagorodnova, N., et al. 2017, *ApJ*, **842**, 29
- Hunter, J. D. 2007, *Comput. Sci. Eng.*, **9**, 90
- Iben, Jr., I., & Tutukov, A. V. 1985, *ApJS*, **58**, 661
- Inserra, C., Smartt, S. J., Fraser, M., et al. 2012, *ATel*, **4329**, 1
- Ivezic, Z., Axelrod, T., Brandt, W. N., et al. 2008, *Serb. Astron. J.*, **176**, 1
- Jiang, N., Dou, L., Wang, T., et al. 2016, *ApJ*, **828**, L14
- Jiang, N., Wang, T., Dou, L., et al. 2021, *ApJS*, **252**, 32
- Jose, J., Guo, Z., Long, F., et al. 2014, *ATel*, **6777**, 1
- Kalberla, P. M. W., Burton, W. B., Hartmann, D., et al. 2005, *A&A*, **440**, 775
- Khorunzhev, G. A., Sazonov, S. Y., Medvedev, P. S., et al. 2022, *Astron. Lett.*, **48**, 767
- Kochanek, C. S. 2016, *MNRAS*, **461**, 371
- Kochanek, C. S., Shappee, B. J., Stanek, K. Z., et al. 2017, *PASP*, **129**, 104502
- Koljonen, K. I. I., Lioudakis, I., Lindfors, E., et al. 2024, *MNRAS*, **532**, 112
- Krimm, H. A., Kennea, J. A., Holland, S. T., et al. 2011, *ATel*, **3384**, 1
- Kumar, H., Berger, E., Hiramatsu, D., et al. 2024, *ApJ*, **974**, L36
- Law, N. M., Kulkarni, S. R., Dekany, R. G., et al. 2009, *PASP*, **121**, 1395
- Law-Smith, J., Ramirez-Ruiz, E., Ellison, S. L., & Foley, R. J. 2017, *ApJ*, **850**, 22
- Li, R.-L., Yuan, C., He, H.-N., et al. 2024, arXiv e-prints [arXiv:2411.06440]
- Liddle, A. R. 2007, *MNRAS*, **377**, L74
- Lin, D., Carrasco, E. R., Grupe, D., et al. 2011, *ApJ*, **738**, 52
- Lin, Z., Jiang, N., Wang, T., et al. 2024, *ApJ*, **971**, L26
- Liu, C., Yazar, R., & Ramirez-Ruiz, E. 2025, *ApJ*, **979**, 40
- Magnier, E. A., Chambers, K. C., Flewelling, H. A., et al. 2020a, *ApJS*, **251**, 3
- Magnier, E. A., Schlafly, E. F., Finkbeiner, D. P., et al. 2020b, *ApJS*, **251**, 6
- Magnier, E. A., Sweeney, W. E., Chambers, K. C., et al. 2020c, *ApJS*, **251**, 5
- Magorrian, J., & Tremaine, S. 1999, *MNRAS*, **309**, 447
- Mainetti, D., Lupi, A., Campana, S., & Colpi, M. 2016, *MNRAS*, **457**, 2516
- Mainzer, A., Bauer, J., Grav, T., et al. 2011, *ApJ*, **731**, 53
- Mainzer, A., Bauer, J., Cutri, R. M., et al. 2014, *ApJ*, **792**, 30
- Makrygianni, L., Arcavi, I., Newsome, M., et al. 2025, *ApJ*, **987**, L20
- Mandel, I., & Levin, Y. 2015, *ApJ*, **805**, L4
- Masci, F. J., Laher, R. R., Rusholme, B., et al. 2019, *PASP*, **131**, 018003
- Masterson, M., De, K., Panagiotou, C., et al. 2024, *ApJ*, **961**, 211
- Merloni, A., Lamer, G., Liu, T., et al. 2024, *A&A*, **682**, A34
- Miller, J. M., Kaastra, J. S., Miller, M. C., et al. 2015, *Nature*, **526**, 542
- Mockler, B., Gallegos-Garcia, M., Göteborg, Y., Miller, J. M., & Ramirez-Ruiz, E. 2024, *ApJ*, **973**, L9
- Monet, D. G., Levine, S. E., Canzian, B., et al. 2003, *AJ*, **125**, 984
- Moretti, A., Campana, S., Mineo, T., et al. 2005, *SPIE Conf. Ser.*, **5898**, 360
- Munoz-Arancibia, A., Hernandez-Garcia, L., Bauer, F. E., et al. 2023, *Transient Name Server AstroNote*, **138**, 1
- Nevalainen, J., Markevitch, M., & Lumb, D. 2005, *ApJ*, **629**, 172
- Newsome, M., Arcavi, I., Dgany, Y., & Pellegrino, C. 2022, *Transient Name Server AstroNote*, **236**, 1

- Newsome, M., Arcavi, I., Howell, D. A., et al. 2024, *ApJ*, 977, 258
- Nicholl, M., Blanchard, P. K., Berger, E., et al. 2019, *MNRAS*, 488, 1878
- Nicholl, M., Wevers, T., Oates, S. R., et al. 2020, *MNRAS*, 499, 482
- Nicholl, M., Lanning, D., Ramsden, P., et al. 2022, *MNRAS*, 515, 5604
- Oke, J. B., & Gunn, J. E. 1983, *ApJ*, 266, 713
- Onori, F., Cannizzaro, G., Jonker, P. G., et al. 2022, *MNRAS*, 517, 76
- Paczyński, B. 1967, *Acta Astron.*, 17, 355
- Paggi, A., Massaro, F., D'Abrusco, R., et al. 2013, *ApJS*, 209, 9
- Panagiotou, C., De, K., Masterson, M., et al. 2023, *ApJ*, 948, L5
- Pasham, D. R., Cenko, S. B., Sadowski, A., et al. 2017, *ApJ*, 837, L30
- Pasham, D. R., Lucchini, M., Laskar, T., et al. 2023, *Nat. Astron.*, 7, 88
- Perri, M., Maselli, A., Giommi, P., et al. 2007, *A&A*, 462, 889
- Pfahl, E. 2005, *ApJ*, 626, 849
- Poidevin, F., Pérez-Fournon, I., Geier, S., et al. 2023, *Transient Name Server Classification Report*, 2023-3050, 1
- Prieto, J. L., Bersier, D., Holoien, T. W. S., et al. 2014, *ATel*, 5831, 1
- Puccetti, S., Capalbi, M., Giommi, P., et al. 2011, *A&A*, 528, A122
- Rau, A., Kulkarni, S. R., Law, N. M., et al. 2009, *PASP*, 121, 1334
- Rees, M. J. 1988, *Nature*, 333, 523
- Reis, R. C., Reynolds, M. T., Miller, J. M., Miller, B. P., & Hadjiyska, E. 2012, *ATel*, 4346, 1
- Roming, P. W. A., Kennedy, T. E., Mason, K. O., et al. 2005, *Space Sci. Rev.*, 120, 95
- Saxton, R. D., Read, A. M., Komossa, S., et al. 2019, *A&A*, 630, A98
- Saxton, R., Komossa, S., Auchettl, K., & Jonker, P. G. 2020, *Space Sci. Rev.*, 216, 85
- Sazonov, S., Gilfanov, M., Medvedev, P., et al. 2021, *MNRAS*, 508, 3820
- Scargle, J. D. 1998, *ApJ*, 504, 405
- Scargle, J. D., Norris, J. P., Jackson, B., & Chiang, J. 2013, *ApJ*, 764, 167
- Schlafly, E. F., & Finkbeiner, D. P. 2011, *ApJ*, 737, 103
- Shappee, B. J., Prieto, J. L., Grupe, D., et al. 2014, *ApJ*, 788, 48
- Shingles, L., Smith, K. W., Young, D. R., et al. 2021, *Transient Name Server AstroNote*, 7, 1
- Short, P., Lawrence, A., Nicholl, M., et al. 2023, *MNRAS*, 525, 1568
- Smartt, S. J., Inserra, C., Fraser, M., et al. 2012, *ATel*, 4299, 1
- Smith, K. W., Smartt, S. J., Young, D. R., et al. 2020, *PASP*, 132, 085002
- Somalwar, J. J., Ravi, V., Dong, D. Z., et al. 2025a, *ApJ*, 982, 163
- Somalwar, J. J., Ravi, V., Yao, Y., et al. 2025b, *ApJ*, 985, 175
- Stein, R., van Velzen, S., Kowalski, M., et al. 2021, *Nat. Astron.*, 5, 510
- Stokes, G. H., Evans, J. B., Vighh, H. E. M., Shelly, F. C., & Pearce, E. C. 2000, *Icarus*, 148, 21
- Stone, N. C., & Metzger, B. D. 2016, *MNRAS*, 455, 859
- Subrayan, B. M., Milisavljevic, D., Chornock, R., et al. 2023, *ApJ*, 948, L19
- Sun, L., Jiang, N., Dou, L., et al. 2024, *Recurring tidal disruption events a decade apart in IRAS F01004-2237*
- Syer, D., & Ulmer, A. 1999, *MNRAS*, 306, 35
- Tadhunter, C., Spence, R., Rose, M., Mullaney, J., & Crowther, P. 2017, *Nat. Astron.*, 1, 0061
- Tonry, J. L., Denneau, L., Heinze, A. N., et al. 2018, *PASP*, 130, 064505
- van Velzen, S., Farrar, G. R., Gezari, S., et al. 2011, *ApJ*, 741, 73
- van Velzen, S., Anderson, G. E., Stone, N. C., et al. 2016, *Science*, 351, 62
- van Velzen, S., Gezari, S., Hammerstein, E., et al. 2021, *ApJ*, 908, 4
- Virtanen, P., Gommers, R., Oliphant, T. E., et al. 2020, *Nat. Methods*, 17, 261
- Wang, J., & Merritt, D. 2004, *ApJ*, 600, 149
- Wang, Y., Jiang, N., Wang, T., et al. 2022, *ApJ*, 930, L4
- Waters, C. Z., Magnier, E. A., Price, P. A., et al. 2020, *ApJS*, 251, 4
- Webb, N. A., Coriat, M., Traulsen, I., et al. 2020, *A&A*, 641, A136
- Wevers, T., Pasham, D. R., van Velzen, S., et al. 2019, *MNRAS*, 488, 4816
- Wevers, T., Nicholl, M., Guolo, M., et al. 2022, *A&A*, 666, A6
- Wevers, T., Coughlin, E. R., Pasham, D. R., et al. 2023, *ApJ*, 942, L33
- Wright, E. L., Eisenhardt, P. R. M., Mainzer, A. K., et al. 2010, *AJ*, 140, 1868
- Wyrzykowski, Ł., Zieliński, M., Kostrzewa-Rutkowska, Z., et al. 2017, *MNRAS*, 465, L114
- Yao, Y., Ravi, V., Gezari, S., et al. 2023, *ApJ*, 955, L6
- Yaron, O., & Gal-Yam, A. 2012, *PASP*, 124, 668
- York, D. G., Adelman, J., Anderson, Jr., J. E., et al. 2000, *AJ*, 120, 1579
- Yuan, C., Winter, W., & Lunardini, C. 2024, *ApJ*, 969, 136
- Zauderer, B. A., Berger, E., Soderberg, A. M., et al. 2011, *Nature*, 476, 425
- Zhong, S. 2025, *ApJ*, 983, 131

Appendix A: Published TDEs

AT 2023vto: This object was initially classified (and still is) as a superluminous super nova Type II (SLSN II) by Poidevin et al. (2023). This classification was based on faint H_{β} emission that was detected in optical spectra obtained on 2023-11-21 22:30:53 (UTC). However, Kumar et al. (2024) classified it as a TDE, after identifying the broad emission centred at $\lambda 4511 \text{ \AA}$ (see their Fig. 4) to be a broad, blueshifted He II $\lambda 4686 \text{ \AA}$ emission line (TDE-He; see Sect. 4.2).

AT 2022cmc: This is a jetted TDE (Andreoni et al. 2022; Pasham et al. 2023), similar to Sw J1644 + 57, which unlike the other jetted TDEs, was discovered in optical wavelengths.

AT 2022agi: This is a repeating TDE (see Subsection 4.3), also known as F01004. The first flare was reported in Tadhunter et al. (2017), while the second was studied in Sun et al. (2024).

AT 2020ksf: This TDE was first reported in Gilfanov et al. (2020), where a soft X-ray transient source was found to be coincident with AT 2020ksf. Furthermore, Alexander et al. (2021) reported faint radio emission detections coincident with the objects position.

AT 2017gge: This TDE was first reported in Wang et al. (2022) (ATLAS17jrp) and later appeared in Onori et al. (2022). Recently, it was reported to be the second TDE associated with a high-energy neutrino in Li et al. (2024), following AT 2019dsg (Stein et al. 2021).

AT 2017eqx: This TDE was first reported in Nicholl et al. (2019), with broad H I and H II emission.

LSQ12dyw: This TDE debuted first in a few circulars (Inserra et al. 2012; Smartt et al. 2012; Reis et al. 2012), where its nature was discussed. It was later studied and included in the sample of Charalampopoulos et al. (2022).

PTF09djf, *PTF09ge*: These TDEs were first presented in Arcavi et al. (2014), where they were characterised as TDE candidates. Later, they were included in the TDE sample of Charalampopoulos et al. (2022).

PS1-10jh: This TDE first appeared in Gezari et al. (2012), where its spectroscopic signature showed broad He II emission lines. It was later included in the Charalampopoulos et al. (2022) TDE sample.

iPTF15af: This TDE first appeared in Blagorodnova et al. (2019), with broad He II emission in its optical spectrum and several other broad features in the UV spectrum. It was later included in the Charalampopoulos et al. (2022) TDE sample.

iPTF16axa: This TDE was introduced as a candidate in Hung et al. (2017), where it showed broad hydrogen and helium emission lines. It was later included in the Charalampopoulos et al. (2022) TDE sample.

ASASSN-14li: This TDE was discovered in December of 2014 (Jose et al. 2014) and has since been studied extensively across the electromagnetic spectrum, in X-rays (Miller et al. 2015; Holoien et al. 2016b; Pasham et al. 2017), in the optical and near-UV (Cenko et al. 2016; Holoien et al. 2016b; Pasham et al. 2017), IR (Jiang et al. 2016) and radio (Alexander et al. 2016; van Velzen et al. 2016). It was later included in the Charalampopoulos et al. (2022) TDE sample.

ASASSN-14ae: This TDE was discovered in January of 2014 (Prieto et al. 2014) and was first studied in Holoien et al. (2014) as a candidate, where the initial spectrum showed broad hydrogen emission and later evolved into having both broad helium and hydrogen emission. This source was also included in the Charalampopoulos et al. (2022) TDE sample.

ASASSN-15oi: This TDE was discovered in August of 2015 (Brimacombe et al. 2015) and was studied in Holoien et al.

(2016a), where its optical spectrum showed broad helium features. It was later included in the Charalampopoulos et al. (2022) TDE sample.

Swift J1644+57: First, this source was thought to be a long lasting γ -ray outburst, discovered by the *Swift* BAT instrument. It was later revealed to be a TDE (Burrows et al. 2011; Bloom et al. 2011), since it decayed almost following the TDE characteristic $t^{-5/3}$ power law. Moreover, Zauderer et al. (2011) reported radio detections coincident with this source, shortly after its discovery. The properties of this source led to the conclusion that Swift J1644+57 is a highly beamed, non-thermal, relativistic, jetted X-ray TDE.

Swift J2058+08: This source was detected shortly after the discovery of Swift J1644+57, once again by *Swift* BAT, sharing many similarities with it. It was first reported in Krimm et al. (2011) and further studied in Cenko et al. (2012), where a multi-wavelength follow-up was initiated. Cenko et al. (2012) detected a radio counterpart to the flare, suggesting that Swift J2058+08 is the second non-thermal (relativistic) jetted X-ray TDE.

Appendix B: X-ray data reduction

B.1. *Swift*-XRT

B.1.1. Data reduction

The XRT photon counting (PC) mode data were downloaded from HEASARC¹⁹ data archive, and processed using the XRT-DAS software (Capalbi et al. 2005) developed at the ASI Science Data Center and included in the HEASoft package (v. 6.33.2) distributed by HEASARC, using a procedure similar to that illustrated in Paggi et al. (2013).

For each observation calibrated and cleaned PC mode event files were produced with the XRTPIPELINE task (ver. 0.13.7), also producing exposure maps for each observation. In addition to the screening criteria used by the standard pipeline processing, we applied a further filter to screen background spikes that can occur when the angle between the pointing direction of the satellite and the bright Earth limb is low. In order to eliminate this so called bright Earth effect, due to the scattered optical light that usually occurs towards the beginning or the end of each orbit, we used the procedure proposed by Puccetti et al. (2011) and D'Elia et al. (2013). We monitored the count rate on the CCD border and, through the XSELECT package, we excluded time intervals when the count rate in this region exceeded 40 counts/s. In addition we selected only time intervals with CCD temperatures less than -50° C (instead of the standard limit of -47° C) since contamination by dark current and hot pixels, which increase the low energy background, is strongly temperature dependent (D'Elia et al. 2013).

B.1.2. Source detection and flux estimates

To detect X-ray sources in the 0.3 – 10 keV XRT images, we made use of the XIMAGE detection algorithm DETECT, which locates the point sources using a sliding-cell method. The average background intensity is estimated in several small square boxes uniformly located within the image. The position and intensity of each detected source are calculated in a box whose size maximises the S/N.

For each XRT-PC observation, we considered as coordinates of the X-ray counterpart to the TDE source the coordinates of the detected XRT-PC source closest to the TDE source coordinates

¹⁹ <https://heasarc.gsfc.nasa.gov/>

if this happens to lie closer than $5''^{20}$. If no XRT-PC source was detected closer than $5''$ to the TDE source coordinates, we used the TDE source coordinates themselves.

We then evaluated net 0.3 – 10 keV count rates (or their 3σ upper limits) at X-ray counterpart coordinates with the SOSTA algorithm that, besides the net count rates and the respective uncertainties, yields the statistical significance of each source. In addition, SOSTA also estimates the optimal extraction radius R_{opt} that maximises the S/N of the source. We note that we used count rates produced by SOSTA rather than those given by DETECT because the former are in most cases more accurate, since DETECT uses a global background for the entire image, whereas SOSTA uses a local background.

In order to get a first estimate of fluxes for TDE sources X-ray counterparts, we extracted appropriate arf and rmf files at each source location, making use of the XRTPRODUCTS task. As extraction regions we used circles centred at the X-ray source coordinates and with a radius equal to R_{opt} . Assuming black body model with a temperature of $\sim 5 \times 10^5 \text{ K}^{21}$ and an absorption component fixed to the Galactic value (Kalberla et al. 2005), we then converted the net 0.3–10 keV count rates evaluated earlier in 0.3–10 keV observed intrinsic (i.e. unabsorbed) fluxes.

B.1.3. Spectral extraction

To obtain better estimates on the X-ray source fluxes – as well as possible spectra variability – we extracted XRT-PC source spectra for the selected X-ray counterparts to TDE sources.

In general, source spectra – with the corresponding arf and rmf files – were extracted from events with XRTPRODUCTS task, using circular regions centred at the X-ray source coordinates with radii equal R_{opt} , while background spectra were extracted from annuli centred at the X-ray source coordinates, with inner and outer radii equal to $2R_{\text{opt}}$ and $3R_{\text{opt}}$, respectively, excluding nearby detected X-ray sources.

When the source count rate is above $0.5 \text{ counts/s}^{-1}$, the data are significantly affected by pileup in the inner part of the PSF (Moretti et al. 2005). To remove the pile-up contamination, we extract only events contained in an annular region centred on the X-ray source coordinates (Perri et al. 2007). While the outer radius of the annulus was set at R_{opt} , the inner radius was determined by comparing the observed profiles with the updated XRT PSF analytical model²².

B.2. Chandra-ACIS

B.2.1. Data reduction

Chandra-ACIS data were retrieved from the Chandra Data Archive²³, and were processed and analysed with the Chandra Interactive Analysis of Observations (CIAO, Fruscione et al. 2006) data analysis system version 4.16 and Chandra calibration

²⁰ This radius represents a conservative value that includes systematic astrometric uncertainties of the various telescopes, as well as positional uncertainties related to the source fluxes. We checked that the majority of the detected X-ray sources fall at separations well below this value, with 70% of the sources at separations $< 1''$, 85% of the sources at separations $< 2''$, and more than 90% of the sources at separations $< 3''$.

²¹ This value has been evaluated from the error weighted average temperature obtained from the spectral fits, see Appendix B.4

²² https://www.swift.ac.uk/analysis/xrt/SWIFT-XRT-CALDB-10_v01.pdf

²³ <http://cda.harvard.edu/chaser>

database CALDB version 4.11.1, adopting standard procedures. We run the ACIS level 2 processing with CHANDRA_REPRO to apply up-to-date calibrations (CTI correction, ACIS gain, bad pixels), and then excluded time intervals of background flares exceeding 3σ with the DEFLARE task. We produced 0.3 – 7 keV full-band exposure maps, psf maps, and pileup maps with the PILEUP_MAP task.

B.2.2. Source detection and flux estimates

We run the WAVDETECT task to identify point sources in each observation with a $\sqrt{2}$ sequence of wavelet scales (i.e., 1 1.41 2 2.83 4 5.66 8 11.31 16 pixels) and a false-positive probability threshold of 10^{-6} .

As we did for Swift-XRT (see Sect. B.1.2), we considered as coordinates of the X-ray counterpart to the TDE source the coordinates of the detected Chandra-ACIS source closest to the TED source coordinates if this happens to lie closer than $5''$. If no Chandra-ACIS source was detected closer than $5''$ to the TDE source coordinates, we extracted counts at the TDE source coordinates.

To evaluate the source fluxes we made use of the SRCFLUX task, extracting counts from circular regions centered at the source location, with radii equal to the 99% EEFLUX PSF radius R_{99} (as estimated from the PSF maps), while for the background regions we considered annuli with inner and outer radii equal to $2R_{99}$ and $3R_{99}$, respectively, excluding nearby detected X-ray sources. Appropriate arf and rmf files were generated for the considered regions, and the net 0.3 – 7 keV count rates were converted to 0.3 – 10 keV observed intrinsic fluxes assuming a model comprising an absorption component fixed to the Galactic value and a black body with a temperature of $\sim 10^6 \text{ K}$. In the case of unconstrained count rates, 3σ upper limits were evaluated with the APRATES_TOOL task, and converted to intrinsic flux upper limits with the MODELFLUX task, adopting the same model described before.

B.2.3. Spectral extraction

Source spectra and the corresponding arf and rmf files were extracted from event files with SPECSEXTRACT task, using circular regions centred at the X-ray source coordinates with radii equal R_{99} , while background spectra were extracted from annuli centred at the X-ray source coordinates, with inner and outer radii equal to $2R_{99}$ and $3R_{99}$, respectively, excluding nearby detected X-ray sources. Also in this case we excluded inner pixels with pileup larger than 5% as estimated from the pileup maps.

B.3. XMM-Newton-EPIC

B.3.1. Data reduction

XMM-Newton-EPIC data were retrieved from the XMM-Newton Science Archive²⁴ and reduced with the SAS²⁵ 21.0.0 software.

Following Nevalainen et al. (2005) we filtered EPIC data for hard-band flares by excluding the time intervals where the 9.5 – 12 keV (for MOS1 and MOS2) or 10 – 12 keV (for PN) count rate evaluated on the whole detector FOV was more than 3σ away from its average value. To achieve a tighter filtering of background flares, we iteratively repeated this process two

²⁴ <https://www.cosmos.esa.int/web/xmm-newton/xsa>

²⁵ <http://www.cosmos.esa.int/web/xmm-newton/sas>

more times, re-evaluating the average hard-band count rate and excluding time intervals away more than 3σ from this value. The same procedure was applied to soft 1 – 5 keV band restricting the analysis to an annulus with inner and outer radii of 12' and 14' excluding detected X-ray sources in the field, where the detected emission is expected to be dominated by the background.

B.3.2. Source detection and flux estimates

When possible, we merged 0.3 – 10 keV data from MOS1, MOS2 and PN detectors using the EMOSAIC task, in order to detect the fainter sources that would not be detected otherwise. Sources were detected following the standard SAS sliding box task EDETECT_CHAIN that mainly consist of three steps: 1) source detection with local background, with a minimum detection likelihood of 8; 2) remove sources in step 1 and create a smooth background maps by fitting a 2-D spline to the residual image; 3) source detection with the background map produced in step 2 with a minimum detection likelihood of 10. The task EMLDETECT was then used to determine the parameters for each input source – including the count rate – by means of a maximum likelihood fit to the input images, selecting sources with a minimum detection likelihood of 15 and a flux in the 0.3 – 10 keV band larger than 10^{-14} erg cm⁻² s⁻¹ (assuming an energy conversion factor of 1.2×10^{-11} cts cm² erg⁻¹). An analytical model of the PSF was evaluated at the source position and normalised to the source brightness. The source extent R_{ext} was then evaluated as the radius at which the PSF level equals half of local background.

Again, we considered as coordinates of the X-ray counterpart to the TDE source the coordinates of the detected *XMM-Newton*-EPIC source closest to the TDE source coordinates if this happens to lie closer than 5". If no *XMM-Newton*-EPIC source was detected closer than 5" to the TDE source coordinates, we considered as coordinates of the possible X-ray counterpart the TDE source coordinates themselves. In this case, the source 0.3 – 10 keV net count rate (or its 3 σ upper limits) and optimal extraction radius (maximising the signal to noise ratio of the source) was provided by EREGIONALYSE.

Again, to estimate the fluxes of TDE sources X-ray counterparts, we extracted appropriate arf and rmf files for each available detector at each source location, making use of the ARFGEN and RMFGEN tasks. As extraction regions we used circles centred at the X-ray source coordinates and with a radius equal to R_{ext} . Assuming a black body model with a temperature of $\sim 10^6$ K and a absorption component fixed to the Galactic value, we then converted the net 0.3 – 10 keV count rates of each detector 0.3 – 10 keV intrinsic (i.e. unabsorbed) fluxes. The mean source flux was then finally evaluated as the mean of the fluxes of each available detector weighted by its uncertainty, and the uncertainty on this mean flux was evaluated as

$$\bar{\sigma} = \sqrt{1 / \sum_i (1/\sigma_i^2)}, \quad (\text{B.1})$$

where the sum runs on the available detectors (Webb et al. 2020).

B.3.3. Spectral extraction

The source spectra were extracted with the EVSELECT task from circular regions centred at the X-ray source coordinates with radii equal R_{ext} , while background spectra were extracted from annuli centred at the X-ray source coordinates, with inner

and outer radii equal to $2R_{\text{ext}}$ and $3R_{\text{ext}}$, respectively, excluding nearby detected X-ray sources. The corresponding arf and rmf files were generated with the RMFGEN and ARFGEN tasks to take into account time and position-dependent EPIC responses. Again, inner regions of high pileup were estimated and excluded using the *epatplot* task through the distortion of pattern distribution, following the procedure explained in the SAS Data Analysis Threads²⁶.

B.4. X-Ray spectral fitting

Spectral fitting was performed with the Sherpa²⁷ modelling and fitting application (Freeman et al. 2001) in the 0.3 – 10 keV energy range for *Swift*-XRT and *XMM-Newton*-EPIC spectra, and in the 0.3 – 7 keV energy range for *Chandra*-ACIS spectra, adopting Gehrels weighting (Gehrels 1986). Source spectra were binned to a minimum of 20 counts/bin to ensure the validity of χ^2 statistics. In addition, for the EPIC spectra we excluded from the spectral fitting the 1.45 – 1.55 keV band due to variable Al K lines, and fitted simultaneously MOS1, MOS2 and PN spectra, if available.

For the spectral fitting we used two different models: (1) a model comprising an absorption component fixed to the Galactic value and a power-law with slope a and (2) a model comprising an absorption component fixed to the Galactic value and a black body with temperature T_{BB} . In order to select the best fit model we made use of the Akaike information criterion (AIC, see for example Liddle 2007):

$$AIC = \chi^2 + 2k, \quad (\text{B.2})$$

where k is the number of model parameters, so we selected as the best-fit model the one that provides the lower value of AIC.

B.5. X-ray catalogues

B.5.1. XMM catalogue

We cross-matched the 4XMM-DR13 catalogue with our catalogue of TDEs using a 5" search radius. Since the fluxes reported in 4XMM-DR13 are derived from the count rates assuming a model comprising a power-law with slope 1.7 and a Galactic absorption of 3×10^{20} cm⁻² (Webb et al. 2020), for uniformity we converted the 0.2 – 12 keV count rates for each detector to 0.3 – 10 keV observed intrinsic fluxes using PIMMS²⁸, assuming a model comprising an absorption component fixed to the Galactic value and a black body with a temperature of $\sim 10^6$ K. The fluxes for each detector and their respective uncertainties were there converted in mean flux and uncertainty using the same procedure illustrated in Sect. B.3.2.

B.5.2. EROSITA

We cross-matched the eRASS1 catalogue with our catalogue of TDEs using a 5" search radius. The fluxes reported in eRASS1 are derived from the count rates assuming a model comprising a power-law with slope 2.0 and a Galactic absorption of 3×10^{20} cm⁻² (Merloni et al. 2024), and therefore we converted the 0.2 – 5 keV count rates reported in the catalogue

²⁶ <https://www.cosmos.esa.int/web/xmm-newton/sas-thread-epatplot>

²⁷ <http://cxc.harvard.edu/sherpa>

²⁸ <https://heasarc.gsfc.nasa.gov/docs/software/tools/pimms.html>

to 0.3 – 10 keV observed intrinsic fluxes using PIMMS, again assuming a model comprising an absorption component fixed to the Galactic value and a black body with a temperature of $\sim 10^6$ K.

For the TDE sources for which we did not find an eRASS1 counterpart, we obtained eRASS1 upper limits²⁹. The upper limit eRASS 0.2 – 5 keV fluxes were again converted in 0.3 – 10 keV fluxes using PIMMS³⁰.

Appendix C: Archival repeating flares

C.1. AT 2018fyk

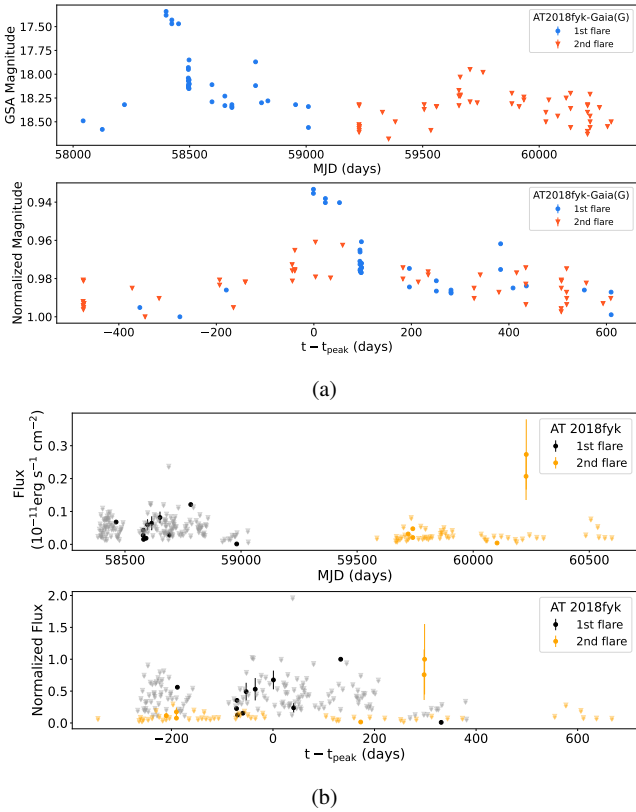


Fig. C.1: Archival optical and X-ray light curves of AT 2018fyk. (a) : Same as for Fig. 6 but for the Gaia *G*-band light curve of AT 2018fyk. (b) : Same as Fig. 6 but for the catalogue X-ray data of AT 2018fyk. The black points and orange points show the detections, while the grey and light orange points show the 3σ upper limits.

Appendix D: Repeating flare timescale comparison

To quantitatively investigate the similarity of the flares in the repeating flare sample, we estimate the rise times, decay times, peak flux and duration (metrics) for the non-confirmed TDE flares as well (i.e. first flare of AT 2022agi, first flare of AT 2019azh, first flare of AT 2024pvu, second flare of AT 2021mhg). We note that we were unable to compute the rise time of AT 2021mhg’s second flare due to substantial gaps in the light curves. Additionally, we exclude AT 2018fyk because the second flare is very faint in the optical band. For AT 2022exr and

AT 2021uvz, which are the double peak flares, as well as AT 2020acka, we cannot evaluate the shape of their flares since they are overlapping.

Figure D.1 shows the metrics of the first flare versus the metrics of the second flare. Almost in all cases (except AT 2024pvu in all timescales), the repeating flares are consistent within uncertainty.

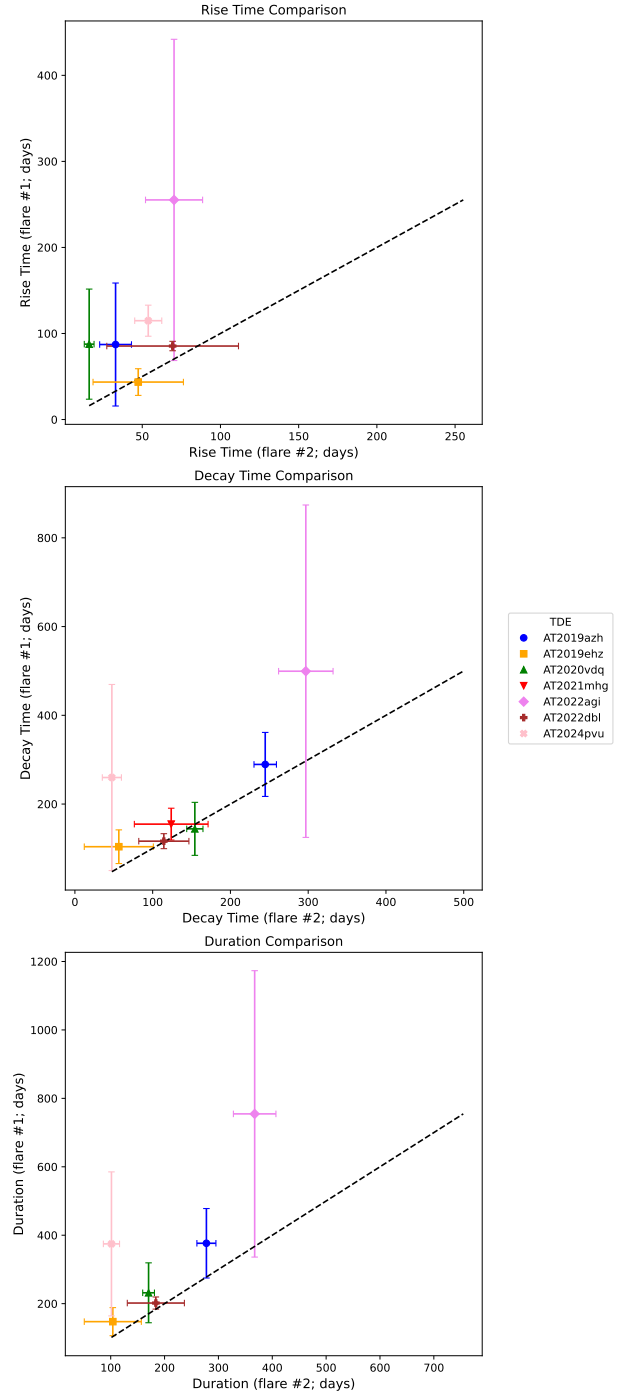


Fig. D.1: Comparison of the timescales for the first and second flares for seven TDEs in our repeating flare sample.

²⁹ https://erosita.mpe.mpg.de/dr1/AllSkySurveyData_dr1/UpperLimitServer_dr1/

³⁰ For the eRASS upper limits in the TDECat GitHub page, we provide the time range covered by the survey, since the exact exposure dates are not provided by the eRASS1 catalogue.